Skoltech

Skolkovo Institute of Science and Technology

MASTER'S THESIS

Machine learning based lake ice detection from Space

Master's Educational Program: Skoltech Space Center

Student

Roberto Aguilar
Skoltech Space Center
May 29, 2020

Research Advisor:

Prof. Dr. Anton Ivanov
Skoltech Space Center

Co-Advisor:

Manu Tom, Dr. Emmanuel Baltsavias, Dr. Silvan Leinss,
Prof. Dr. Konrad Schindler
ETH Zurich

Moscow 2020

Contents

1 Introduction **11**

2 Theoretical Principles **15**

2.1 ESA Sentinel Satellite Program 15

2.1.1 Sentinel-1 Constellation 16

2.1.2 Sentinel-2 Constellation 16

2.2 Synthetic Aperture Radar 16

2.2.1 Signal processing 18

2.2.2 Acquisition Modes 18

2.2.3 ESA SENTINEL-1 data products 19

2.2.4 Radar Backscattering at different surfaces 22

2.3 Multispectral Instrument 25

2.3.1 ESA SENTINEL-2 data products 25

2.3.2 Tiles 26

2.4 Google Earth Engine 26

2.4.1 Sentinel-1 SAR GRD 27

2.4.2 Thermal noise reduction 27

2.4.3 Radiometric calibration 28

2.4.4 Terrain correction 29

2.5 Introduction to Machine Learning Models 31

2.5.1 Support Vector Machine (SVM) 31

2.5.2 Convolutional Neural Networks 31

2.5.3 Semantic Segmentation 33

3 Related work **35**

4 Data **37**

4.1 Sentinel-1 37

4.2 Sentinel-2. 39

5 Methodology **41**
5.1 Sentinel 1 . . . 41
5.2 Sentinel 2 . . . 42
5.3 Sentinel 1+2 System . . . 42

6 Experiments & Results **43**
6.1 Quantitative results . . . 43
6.1.1 Leave one-winter out CV . . . 43
6.1.2 Leave one-lake out CV . . . 46
6.2 Qualitative analysis. . . . 50
6.3 Time-series. . . . 52
6.4 Miscellaneous experiments SAR . . . 57

7 Conclusions and Outlook **58**

A Appendices **64**
A.1 Wind measurements . . . 64
A.2 Detailed experimentation Sentinel-1 . . . 67
A.3 Detailed experimentation Sentinel-2 . . . 70
A.4 Summary of daily results for all monitoring data and lakes Sihl, Sils, Silvaplana, and St. Mortiz in the winters 2016-17 and 2017-18 . . . 73

List of Figures

1.1 Examples of RGB composites of Sentinel-1 SAR data (RGB = [*VV, VH, 0*]) of lake St. Moritz showing the lake in the four different states specified in the sub-captions. 12

2.1 Sentinel Program (Status of ESA Earth Observation Programmes 2017). 17
2.2 Sentinel-1 and Sentinel-2 constellations revisit scenario 17
2.3 Summary of SAR processing steps where the range compressed data result from a convolution of the raw data with the range reference function. In a second step the azimuth compression is performed through a convolution with the azimuth reference function, which changes from near to far range. Here the "$*$" represents the convolution operation. 19
2.4 Sentinel-1 Mode, Polarisation, and Observation Geometry [1]. 20
2.5 Different acquisition modes of the Sentinel-1 satellites 20
2.6 Graphical Representation of Sentinel-1 Core Products 21
2.7 Orbits with different incident angle on the same point on Earth [2]. 23
2.8 Polarisations in different planes 24
2.9 Sentinel 2 tiles in UTM/WGS84 projection. Lake Sihl (shown as purple filled rectangle) in corresponds to 32TMT, and lakes in Region Sils shown as yellow filled rectangle) correspond to 32TNS. 26
2.10 Left: Slant range scale distortion, middle: Foreshortening, right: Layover 30
2.11 SVM hyperplane in a binary classification. 32
2.12 Example of the structure of Convolutional Neural Network [3] 32
2.13 Semantic Segmentation of the lake Sihl (Red: non-frozen, Blue: frozen) on top of a RGB image from Sentinel 2, on a transition day from non-frozen to frozen (31/12/2017). 33

4.1 Location of the two regions of study with their corresponding Sentinel-1 orbits and directions (*ascending* or *descending*). Lake Sihl shown in yellow, Region Sils shown in blue. Flight paths were obtained from [4]. 38

4.2 Distribution of frozen and non-frozen pixels for VV and VH polarisations (combined data from lakes Sihl, Sils, Silvaplana and St. Moritz along 2 winters). . . . 39

5.1 *Deeplab v3+* architecture. 42

6.1 Precision-recall curves for lakes Sihl, Sils, Silvaplana, and St. Moritz. The *iso-f*1 curve connects all points in the precision/recall space whose $F1$ scores are the same. Sentinel-1 data of a lake from two winters ($2016-17$ and $2017-18$) forms the test set for a model trained on the data from the other two lakes in both winters. 49

6.2 Qualitative results for lake Sihl on a non-frozen day (row 1), lake Sils on a frozen day (row 2), and lake Silvaplana on a non-frozen day with clouds (row 3), and lake St. Moritz on a frozen day with a shadow on top. For each lake we show the Sentinel-1 composite image (column 1), the ground truth (column 2), the predicted probability map from Deeplab (column 3), and the corresponding binary classification map (column 4). Additionally, column 5 shows the corresponding prediction from SVM, and in column 6 Sentinel-2 image for better visual interpretation. 50

6.3 Correlation of our results (winter $2016-17$) on lake Sihl with the ground truth and the auxiliary temperature data. 53

6.4 Correlation of our results (winter $2017-18$) on lake Sihl with the ground truth and the auxiliary temperature data. 53

6.5 Correlation of our results (winter $2016-17$) on lake Sils with the ground truth and the auxiliary temperature data. 54

6.6 Correlation of our results (winter $2017-18$) on lake Sils with the ground truth and the auxiliary temperature data. 55

6.7 Correlation of our results (winter $2016-17$) on lake St. Moritz with the ground truth and the auxiliary temperature data. 56

6.8 Correlation of our results (winter $2017-18$) on lake St. Moritz with the ground truth and the auxiliary temperature data. 56

A.1 Wind measurements at 05:20 and 17:20 UTC from Samedan station for winters 2016-17 and 2017-18 65

A.2 Distribution of frozen and non-frozen pixels for VV and VH polarisations in different wind speed condtions on Region Sils, along 2 winters. Best if viewed on screen. 66

List of Tables

1.1 Characteristics of the four target lakes. Altitude (L) and altitude (S) denote the altitudes of the lake and the nearest meteo station respectively. The distance to the station is also shown. 13

2.1 Different frequency bands with frequency and wavelength (Moreira et al, 2013). 18
2.2 Main characteristics of the four different acquisition modes: Stripmap (SW), Interferometric Wide Swath (IW), Extra Wide Swath (EW), and Wave (WV). . 19
2.3 Estimated relative permittivity in Farads per meter (F/m) for different materials [5]. 24
2.4 Sentinel-2 MSI: MultiSpectral Instrument, Level-1C. Resolution is given in meters (m), Wavelenght in nanometers (nm) 25

4.1 Dataset statistics for Sentinel 1 and Sentinel 2, shown as (S1 / S2). The non-transition days, on which a lake is fully frozen or fully non-frozen, and transition days (partially frozen dates) are shown. For S1 all available observations are available in the table, for Sentinel 2, only observations with cloudiness less than 30% per lake. *acq.* denotes the number of acquisitions along the winter, *lake pixels* the number of pixels corresponding to each lake per observation. 37
4.2 Details of the orbits scanning *Region Sils* (lakes Sils, Silvaplana, St. Moritz) and lake Sihl, such as orbit number, flight direction, scan start time in Universal Coordinate Time (UTC), and approximate incidence angle. 38
4.3 Temporal resolution of different sensors and an integrated system. *S1* contains all SAR images, *S2 (clear only)* contains the count of the images with cloudiness $<$ 70%, S1+S2 contains the count of *S1 + S2 (clear only)*, and *S1 + S2 (all images)* contains the count *S1+S2*. When combining both *S1* and *S2*, the intersection of both sensors on the same day in counted just as 1. 39

6.1 Leave one winter out cross validation on Sentinel-1. Top: Results on 2016-17, trained on 2017-18, Bottom: Results on 2017-18, trained on 2016-17. Total units are in millions of pixels, except for precision, recall, and **accuracy** (bottom right cell in each table). 44
6.2 Per-class- and mean IoU values of frozen and non-frozen classes for each lake. Sentinel-1 data of a lake from winter $2016-17$ is tested using a model trained on the data lakes from all lakes in $2017-18$. 44
6.3 Leave one winter out cross validation on Sentinel-2. Top: Results on 2016-17, trained on 2017-18, Bottom: Results on 2017-18, trained on 2016-17, with a balanced dataset (number of -non-frozen pixels is equal to the number of frozen pixels). Total units are in millions of pixels, except for precision, recall, and **accuracy** (bottom right cell in each table). 45
6.4 Per-class- and mean IoU values of frozen and non-frozen classes for each lake. Sentinel-2 data of a lake from winter $2016-17$ is tested using a model trained on the data lakes from all lakes in $2017-18$, with a balanced dataset (number of -non-frozen pixels is equal to the number of frozen pixels). 45
6.5 Results on **Sentinel-1** for lakes Sihl, Sils, Silvaplana, and St. Moritz. Confusion matrices are shown for the **leave-one-lake-out** cross-validation experiment. Units are in millions of pixels, except for precision, recall, and **accuracy** (bottom right cell in each table). 47
6.6 Per-class and **mean IoU** values of frozen and non-frozen classes for each lake. **Sentinel-1** data of a lake from winter $2016-17$ is tested using a model trained on the data lakes from all lakes in $2017-18$. 47
6.7 Results on **Sentinel-2** for lakes Sihl, Sils, Silvaplana, and St. Moritz. Confusion matrices are shown for the **leave-one-lake-out** cross-validation experiment. Units are in millions of pixels, except for precision, recall, and **accuracy** (bottom right cell in each table). 48
6.8 Per-class and **mean IoU** values of frozen and non-frozen classes for each lake. **Sentinel-2** data of a lake from winter $2016-17$ is tested using a model trained on the data lakes from all lakes in $2017-18$. 48

6.9 Dataset statistics. The non-transition days, on which a lake is fully frozen or fully non-frozen, and transition days (partially frozen dates) are shown. S1 contains results per day from Sentinel-1, with a median filter with K=3. S1+S2 contains results per day combining Sentinel-1 and Sentinel-2, with a median filter with K=3. Highligheted in green are shown the predictions with ±3 days from the ground truth (GT). 52
6.10 Per-class- and mean IoU values of frozen and non-frozen classes with different polarisations. Data from all the four lakes from winter $2016-17$ was tested using a model trained on the data from all four lakes from winter $2017-18$. . . 57

A.1 Results from Sentinel-1 of different training sets with validation on lake Sihl during winter 2016-17. Each row contains results per every training set with $40K$ steps during training process. *NF* stands for Non-frozen and *F* for frozen. Best mIoU in green, worst mIoU in red. 67
A.2 Resultson Sentinel-1 of different training sets with validation on lake Sihl during winter 2017-18. *NF* stands for Non-frozen and *F* for frozen. Best mIoU in green, worst mIoU in red. 67
A.3 Resultson Sentinel-1 of different training sets with validation on lake Sils during winter 2016-17. *NF* stands for Non-frozen and *F* for frozen. Best mIoU in green, worst mIoU in red. 67
A.4 Results from Sentinel-1 of different training sets with validation on lake Sils during winter 2017-18. *NF* stands for Non-frozen and *F* for frozen. Best mIoU in green, worst mIoU in red. 68
A.5 Results from Sentinel-1 of different training sets with validation on lake Silvaplana during winter 2016-17. *NF* stands for Non-frozen and *F* for frozen. Best mIoU in green, worst mIoU in red. 68
A.6 Results from Sentinel-1 of different training sets with validation on lake Silvaplana during winter 2017-18. *NF* stands for Non-frozen and *F* for frozen. Best mIoU in green, worst mIoU in red. 68
A.7 Results from Sentinel-1 of different training sets with validation on lake St. Moritz during winter 2016-17. *NF* stands for Non-frozen and *F* for frozen. Best mIoU in green, worst mIoU in red. 69
A.8 Results from Sentinel-1 of different training sets with validation on lake St. Moritz during winter 2017-18. *NF* stands for Non-frozen and *F* for frozen. Best mIoU in green, worst mIoU in red. 69

A.9 Results from Sentinel-2 of different training sets with validation on lake Sihl during winter 2016-17. *NF* stands for Non-frozen and *F* for frozen. Best mIoU in green, worst mIoU in red. 70
A.10 Results of different training sets with validation on lake Sils during winter 2016-17. *NF* stands for Non-frozen and *F* for frozen. Best mIoU in green, worst mIoU in red. 70
A.11 Results of different training sets with validation on lake Silvaplana during winter 2016-17. *NF* stands for Non-frozen and *F* for frozen. Best mIoU in green, worst mIoU in red. 70
A.12 Results from Sentinel-2 of different training sets with validation on lake St. Moritz during winter 2016-17. *NF* stands for Non-frozen and *F* for frozen. Best mIoU in green, worst mIoU in red. 71
A.13 Results from Sentinel-2 of different training sets with validation on lake Sihl during winter 2017-18. *NF* stands for Non-frozen and *F* for frozen. Best mIoU in green, worst mIoU in red. 71
A.14 Results from Sentinel-2 of different training sets with validation on lake Sils during winter 2017-18. *NF* stands for Non-frozen and *F* for frozen. Best mIoU in green, worst mIoU in red. 71
A.15 Results from Sentinel-2 of different training sets with validation on lake Silvaplana during winter 2017-18. *NF* stands for Non-frozen and *F* for frozen. Best mIoU in green, worst mIoU in red. 72
A.16 Results from Sentinel-2 of different training sets with validation on lake St. Moritz during winter 2017-18. *NF* stands for Non-frozen and *F* for frozen. Best mIoU in green, worst mIoU in red. 72
A.17 Prediction per day: Sihl 2016-17 73
A.18 Prediction per day: Sihl 2017-18 75
A.19 Prediction per day: Sils 2016-17 78
A.20 Prediction per day: Sils 2017-18 82
A.21 Prediction per day: Silvaplana 2016-17 88
A.22 Prediction per day: Silvaplana 2017-18 92
A.23 Prediction per day: St. Moritz 2016-17 97
A.24 Prediction per day: St. Moritz 2017-18 101

Chapter 1

Introduction

Climate change is one of the main challenges humanity is facing today, calling for new methods to quantify and monitor the rapid change in global and local climatic conditions. Various lake observables are related to those conditions and provide an opportunity for long-term monitoring, among them, the duration and extent of lake ice. Remote sensing of lake ice also fits well with the Climate Change Initiative (CCI+, 2017) by the European Space Agency (ESA), where *lakes* and *lake ice* were newly included. Additionally, CCI+ promotes long-term trend studies and climate studies, as recognised by the Global Climate Observing System (GCOS). Furthermore, lake ice influences various economic and social activities, such as winter sports and tourism, hydroelectric power, fishing, transportation, and public safety (e.g., winter and spring flooding due to ice jams). In addition, its impact on the regional environment and ecological systems is significant, which further underlines the need for detailed monitoring.

Satellites are a secure source for remote sensing of the Cryosphere and for sustainable, reliable and long term trend analysis. Additionally, satellite images are currently the only means to monitor large regions systematically and with short update cycles. This increasing importance of satellite observations has also been recognised by the GCOS. Recently, a machine learning-based semantic segmentation approach for lake ice detection using low spatial-resolution (250m-1000m) optical satellite data (MODIS and VIIRS) was proposed [6]. Although the nominal temporal resolution of those sensors is very good (daily coverage), the main drawback of this methodology is frequent data loss due to clouds, which reduces the effective temporal resolution. This is critical, since important phenological variables depend on frequent, reliable observation. In particular, the *ice-on* date is defined as the first day when the lake surface is (almost) completely frozen and remains frozen on the next day, and *ice-off* is defined symmetrically as the first day where a significant amount of the surface is liquid water, and remains in that state for another day [7]. The GCOS accuracy requirement for these two dates is ± 2 days. Systems based on optical satellite data will fail to determine these key events if they coincide with a cloudy period. Moreover, low spatial resolution of MODIS and VIIRS is also a bottleneck for spatially explicit ice mapping. Higher resolution optical sensors like

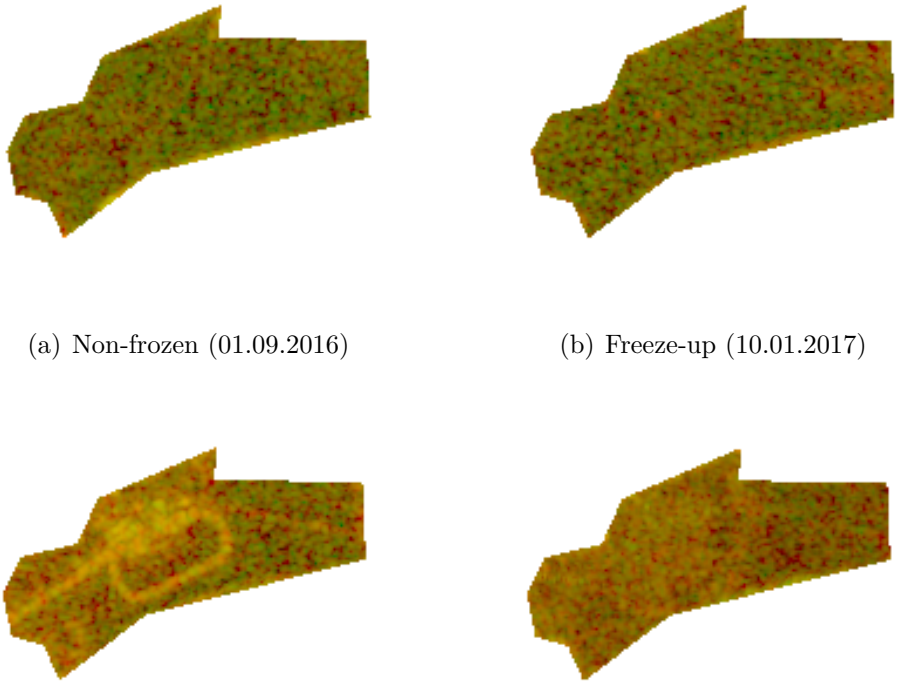

(a) Non-frozen (01.09.2016) (b) Freeze-up (10.01.2017)

(c) Snow with skate tracks (08.02.2017) (d) Break-up (23.03.2017)

Figure 1.1: Examples of RGB composites of Sentinel-1 SAR data (RGB = [*VV, VH, 0*]) of lake St. Moritz showing the lake in the four different states specified in the sub-captions.

Landsat-8 or Sentinel-2 do not provide a solution, due to their low temporal resolution and susceptibility to clouds. On the contrary, Sentinel-1 represents a favourable trade-off between spatial and temporal resolution. Additionally, Radar is unaffected by clouds, which in many regions is a considerable advantage. Here we propose combined Sentinel-1 SAR and Sentinel-2 system, which meets the requirements of lake ice monitoring, and additionally comes for free and with a commitment to ensure continuity of the observations. Its spatial and temporal resolution (GSD ca. 10 m / revisit rate 1-3 days) make it possible to derive high-resolution ice maps almost on a daily basis. For completeness, we mention that, taking into account estimation uncertainty, the temporal resolution of Sentinel-1 falls just short of the 2-day requirement of GCOS, still it can provide an excellent "observation backbone" for an operational system that could fill the gaps with optical satellite data [6] or webcams [8].

Converting a Sentinel-1 image to a lake ice map boils down to 2-class semantic segmentation, i.e., assigning each lake pixel to one of two classes, *frozen* or *non-frozen*. We do this with the *Deeplab v3+* semantic segmentation network [9]. Examples of Sentinel-1 SAR composites over the lake St. Moritz is visualised in Fig. 1.1, showing the VV amplitude in the red channel, and the VH amplitude in the green channel. The examples include the states

non-frozen (01.09.2016, water), *freeze-up* (10.01.2017), *frozen* (08.02.2017, snow on top of ice) and a *break-up* date (23.03.2017). In order to increase the temporal resolution of the system, Sentinel-2 was added with the aim to fill gaps between Sentinel-1 observations or integrate decisions from a single day with data from 2 satellites, performing a pixel-wise classification from Sentinel-2 using a non-deep learning approach with SVMs.

Target lakes and winters. We analyse three selected lakes in Switzerland (*Sihl, Sils, Silvaplana, St. Moritz*, see Table 1.1) over the period of two winters ($2016-17$ and $2017-18$). Sihl is located in the middle of the country, near the Apls, it has a dam which regulates the amount of water it contains, and it doesn't freeze during the whole winter. The three other lakes are located close to each other in the same geographic region, referred to as *Region Sils*. The lakes are comparatively small and situated in an Alpine environment, and they are known to reliably freeze over completely every year during the winter months. For the two winters $2016-2017$ and $2017-2018$, all available images were collected for the nine months between September 1 and May 31. After back-projecting the digitised lake outlines from Open Street Map (OSM) on to the SAR images, for each lake, we extract the the *lake pixels* which lie inside the polygon derived from the lake outline. In low-spatial resolution satellite images such as *MODIS* and *VIIRS*, only few such *lake pixels* are available [6] making the analysis of very small lakes such as St. Moritz difficult or even impossible, but thanks to the higher spatial resolution, the Sentinel-1 time series provides us with millions of lake pixels, which makes it possible to train powerful deep learning models for segmentation, which are extremely data-hungry.

Contributions. We address the problem of lake ice detection from Sentinel-1 SAR data, as an alternative to optical satellite data which is impaired by clouds. In the process, we show that a deep learning model pre-trained on an optical RGB dataset can nevertheless be re-used successfully as initialisation for fine-tuning to Radar data. To our knowledge, our work is the first one that utilises Radar data and deep learning for lake ice detection.

Table 1.1: Characteristics of the four target lakes. Altitude (L) and altitude (S) denote the altitudes of the lake and the nearest meteo station respectively. The distance to the station is also shown.

	Sihl	**Sils**	**Silvaplana**	**St. Moritz**
Area (km^2)	11.3	4.1	2.7	0.78
Altitude (L) (m)	889	1797	1791	1768
Max. depth (m)	17	71	77	42
Meteo station	Einsielden	Segl Maria	Segl Maria	Samedan
Dist. to lake (km)	1.5	0.5	1	5
Altitude (S) (m)	882	1804	1804	1709

The chapter 2 begins with a description of the Sentinel satellite constellation for Earth

Observation, an overview of the Google Earth Engine platform, and the basic concepts of convolutional neural networks (CNNs), support vector machines (SVMs), and semantic segmentation. Chapter 3 is where we talk about the related work in terms of environmental monitoring Earth Observations, as well, as previous work for lake-ice segmentation with Radar and optical space-based sensors. Chapter 4 presents the details of the dataset and in-depth analysis of pre-processing the dataset for making it ready for training. All the experiments, insights and evaluation results are provided in the chapter 6 and further conclusion is given in chapter 7.

Chapter 2

Theoretical Principles

The following section summarizes the relevant background information and theoretical principles which are the basis for the better understanding of this thesis. The chapter will cover a brief introduction to the ESA Sentinel program, essential information about the Synthetic Aperture Radar (SAR) and multispectral imagery, Google Earth Engine datasets and preprocessing steps for different remote sensing sensors, and finally a short introduction to deep learning principles.

2.1 ESA Sentinel Satellite Program

The European Space Agency (ESA) is developing a series of next-generation Earth observation missions, on behalf of the joint ESA/European Commission initiative GMES (Global Monitoring for Environment and Security). The goal of the Sentinel program is to replace the current older Earth observation missions which have reached retirement, such as the ERS mission, or are currently nearing the end of their operational life span. This will ensure a continuity of data so that there are no gaps in ongoing studies. The program plans to have at the end seven satellite families in the orbit (Sentinel 1, 2, 3, 4, 5P, 5, 6) whereof three of them have been launched already. The goals of the program are to monitor and to map the surface of the world. The produced data can be used in for emergency mapping, iceberg monitoring, ice condition forecasting at sea, ship detection, climate change monitoring and many other applications, providing robust datasets for all Copernicus services. All data from the Copernicus program are free of charge and can be downloaded from Google Earth Engine platform, processing steps and available products are discussed in Section 2.4. For this thesis, data was gathered from two Sentinel constellations, Sentinel-1 Synthetic Aperture Radar (SAR) and Sentinel-2 Multi-Spectral Instrument (MSI); whose theoretical principals, acquisition modes, and product types are described in and 2.3 respectively.

2.1.1 Sentinel-1 Constellation

This chapter is based on [10] and [11]. Sentinel-1 is an imaging radar mission providing continuous all-weather, day-and-night imagery at C-band. The SENTINEL-1 constellation provides high reliability, improved revisit time, geographical coverage and rapid data dissemination to support operational applications in the priority areas of marine monitoring, land monitoring and emergency services. Sentinel-1 is the first satellite constellation of the Copernicus program of ESA started in 2014. Today, there are two Sentinel-1 satellites (Sentinel-1A and Sentinel-1B) operational in space. Sentinel-1A was launched in April 2014, Sentinel-1B two years later in April 2016. They are both on the same sun-synchronous near polar orbit, sharing the same orbital plane with a 180° orbital phasing difference. The lifetime of these two satellites is planned to be between 7 and 12 years. After this time, they shall be replaced by two new Sentinel-1 satellites (Sentinel-1C and Sentinel-1D). The satellites have a C-SAR system on board which is mounted at the right side of the satellite (referenced to flight direction). The Sentinel-1 satellite has a repeat cycle of 12 days at the equator, giving a cycle time of 6 days with two Sentinel-1 satellites. During these 12 days the satellite is orbiting the Earth within 98.6 min on an altitude of 693 Km. The inclination is 98.18°. The same point on earth is mapped within one repeat cycle several times and the geographical scanning pattern is shown in Fig. 2.2.

2.1.2 Sentinel-2 Constellation

This chapter is based on [12] if nothing else is stated. Two identical SENTINEL-2 satellites operate simultaneously, phased at 180° to each other, in a sun-synchronous orbit at a mean altitude of 786 m. The position of each SENTINEL-2 satellite in its orbit is measured by a dual-frequency Global Navigation Satellite System (GNSS) receiver. Orbital accuracy is maintained by a dedicated propulsion system. This constellation aims aims at monitoring variability in land surface conditions with Multispectral sensors.

2.2 Synthetic Aperture Radar

This chapter is based on [13] if nothing else is stated. The Sentinel-1 satellites use SAR systems. Like a normal radar, this system sends out electromagnetic waves in the GHz range and detects the backscattered echoes of the surface. The main difference to a normal side looking radar is the higher azimuth resolution. A SAR-system is capable to work at different frequency bands. Each band interacts differently with the surface, so they might be use in different applications.

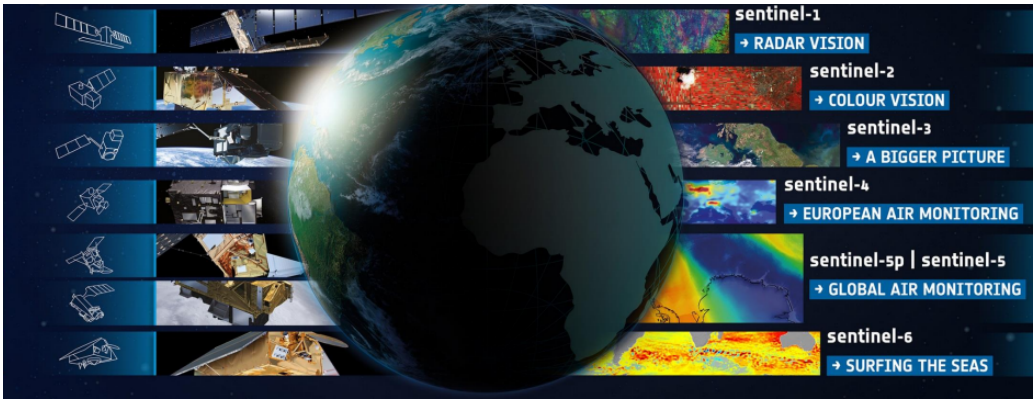

Figure 2.1: Sentinel Program (Status of ESA Earth Observation Programmes 2017).

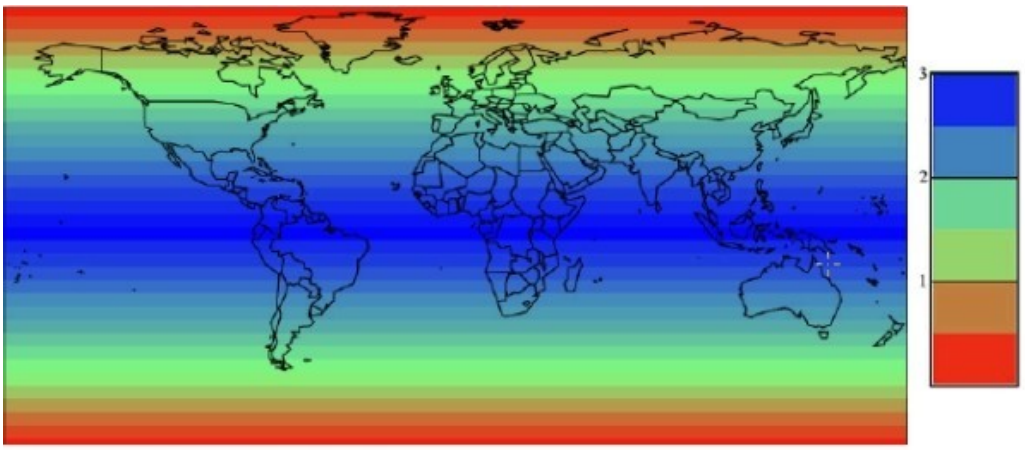

(a) Revisit time of Sentinel 1 constellation (S1A & S1B) updated on May, 2019

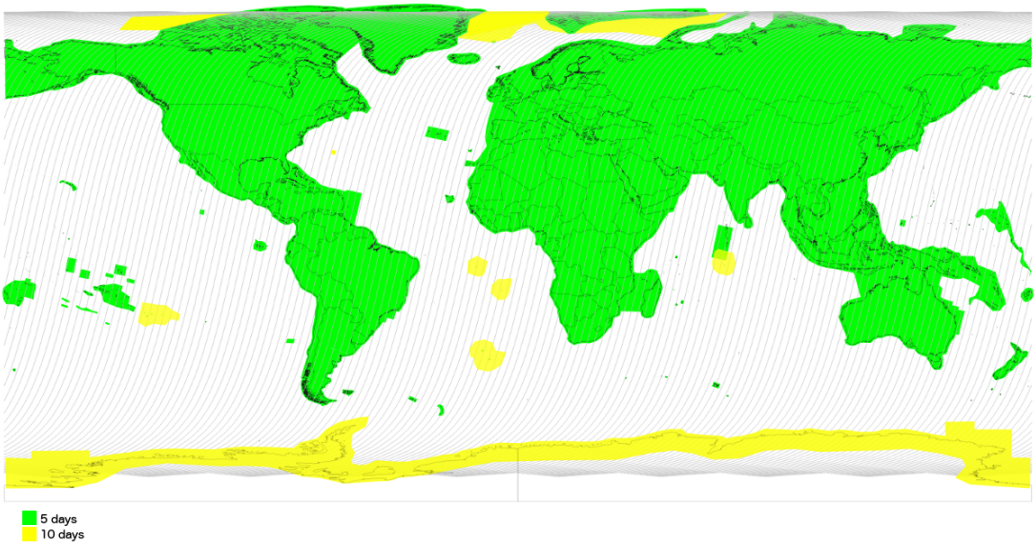

(b) Revisit time of Sentinel 2 constellation (S2A & S2B), updated on October, 2019

Figure 2.2: Sentinel-1 and Sentinel-2 constellations revisit scenario

Table 2.1: Different frequency bands with frequency and wavelength (Moreira et al, 2013).

Frequency Band	**Frequency [GHz]**	**Wavelenght [cm]**
P	0.25-0.5	60-120
L	1-2	15-30
S	2-3.75	8-15
C	3.75-7.5	4-8
X	7.5-12	2.5-4
Ku	12-17.6	1.7-2.5
Ka	25-40	0.75-1.2

Table 2.1 gives an overview about the different available frequency bands. Sentinel-1 operates in the C-frequency band. SAR sensors are using frequency modulated pulse waveforms. That means that the amplitude stays constant, but the frequency is varied. From the reflected signal the SAR sensor measures the amplitude and the phase. A SAR system changes in predefined cycles between transmitting and receiving mode. If the received signals are combined in the right way, it is possible to generate a virtual aperture which is much bigger (based on a given antenna size) and allows to build satellites with smaller antennae. Smaller antennae have also a bigger opening angle which allows to observe the ground on the surface for a longer time than with a normal side looking radar system [14].

2.2.1 Signal processing

The following paragraph is based on [13]. In contrast to visual sensor data, the raw SAR data are not interpretable directly. Figure 2.3 summarizes the necessary transformation process schematically. There are two different, consecutive filter operations used, range followed by azimuth direction. These filter operations are done in the frequency domain and deliver an image which is compressed in the range and the azimuth direction and contains the information about the distance between the satellite and the ground points in the form of reflection intensity data. Five additional correction steps have to be added afterwards in the Google Earth Engine to get suitable, interpretable data (described in 2.4).

2.2.2 Acquisition Modes

This paragraph is based on [15] if nothing else is quoted. There are four different observation modes used by the Sentinel-1 satellites: Stripmap (SM), Inferferometric Wide Swath (IW), Extra Wide Swath (EW), and Wave (WV) . These modes differentiate specifically in their area coverage (Fig. 2.4), with their characteristic listed in Table 2.5. For the purposes of this

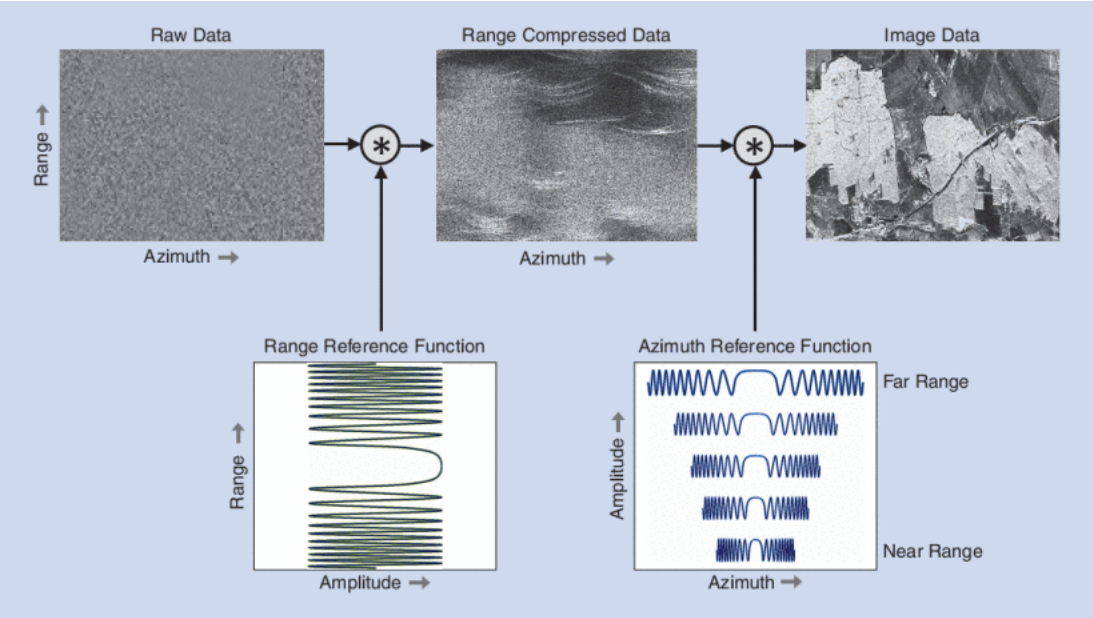

Figure 2.3: Summary of SAR processing steps where the range compressed data result from a convolution of the raw data with the range reference function. In a second step the azimuth compression is performed through a convolution with the azimuth reference function, which changes from near to far range. Here the " $*$ " represents the convolution operation.

Table 2.2: Main characteristics of the four different acquisition modes: Stripmap (SW), Interferometric Wide Swath (IW), Extra Wide Swath (EW), and Wave (WV).

Mode / Characteristic	**SW**	IW	EW	WV
Swath width	80 Km	250 Km	410 Km	Vignette 20 Km x 20 Km
Incidence angle	18.3° - 46.8°	29.1° - 46.0°	18.9° - 47.0°	21.6° - 25.1° 34.8° - 38.0°
Azimuth resolution	5 m	20 m	40 m	5 m
Ground range resolution	5 m	5 m	20 m	5 m
Polarisation option	Dual HH+HV, VV+VH Single HH, VV			Single HH, VV
NESZ	-22 dB			
Default area of operation	Small islands	Land	Sea-ice, polar zones	Open ocean

thesis, IW with VV+VH polarisation was the mode in use, since it was covering land areas corresponding to the region of Switzerland.

2.2.3 ESA SENTINEL-1 data products

ESA offers the data form Sentinel-1 on *Copernicus Open Access Hub*. This web portal offers different customized data product levels from which one can choose. On Google Earth Engine, only Ground Range Detected (GRD) product is available.

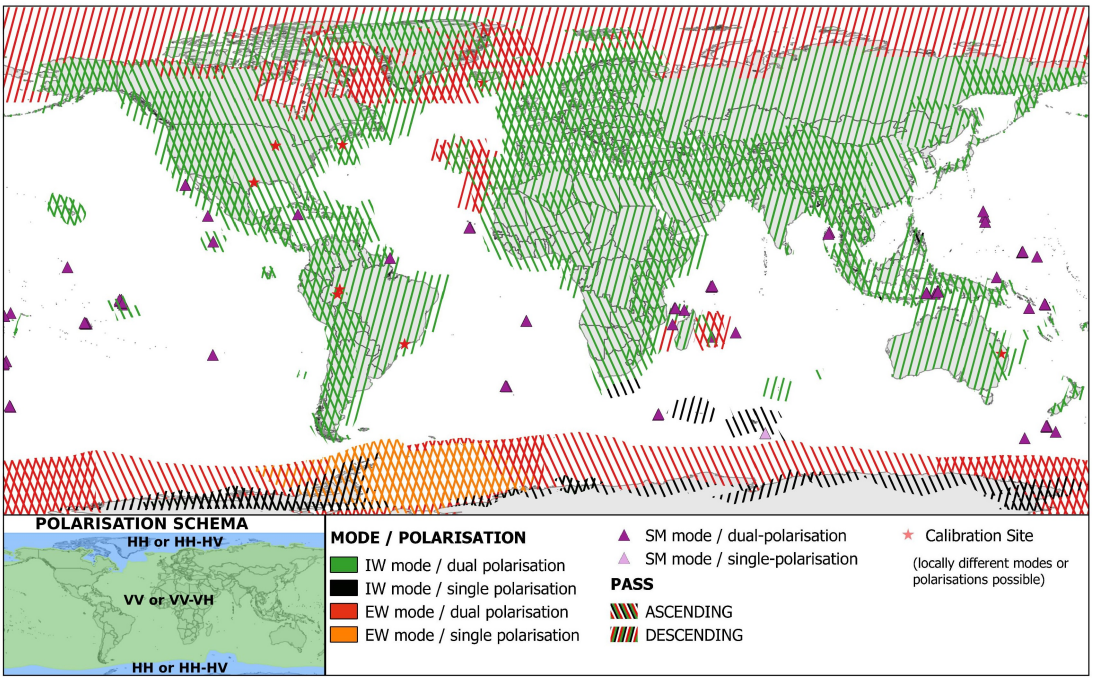

Figure 2.4: Sentinel-1 Mode, Polarisation, and Observation Geometry [1].

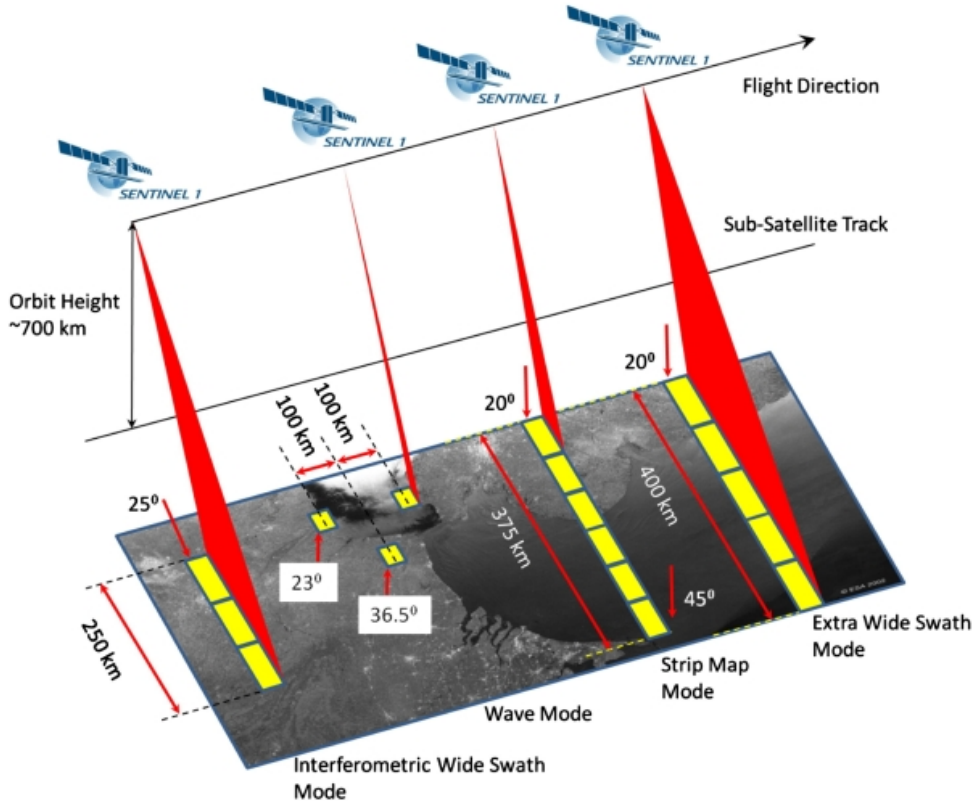

Figure 2.5: Different acquisition modes of the Sentinel-1 satellites

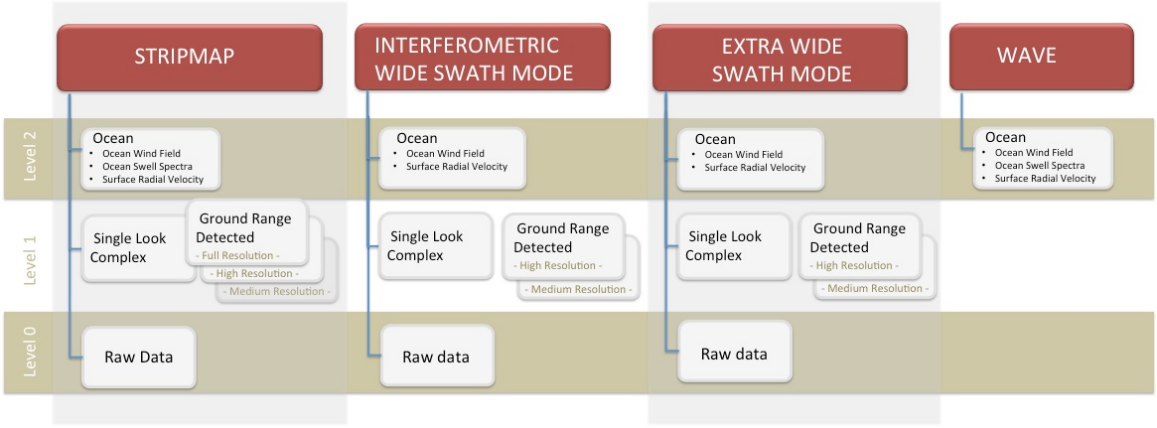

Figure 2.6: Graphical Representation of Sentinel-1 Core Products

- Level 0
  - Raw SAR data contain the compressed and unprocessed instrument source packets, with additional annotations and auxiliary information to support processing. It could be processed with ESA SNAP toolbox.
- Level 1
  - These products are the baseline products for the majority of users from which higher levels are derived. From data in each acquisition mode, the Instrument Processing Facility (IPF) generates focused Level-1 Single Look Complex (SLC) products and Level-1 Ground Range Detected (GRD) products.
    - **Single Look Complex (SLC):** Each pixel is represented by a complex number which contains the whole phase and amplitude information. These images are georeferenced using the orbit information and the altitude of the satellite [16].
    - **Ground Range Detected (GRD):** This product contains data projected to the ground using an Earth ellipsoid. This product has no phase information anymore and has a nearly square spatial resolution. There are different resolutions available: Full Resolution (FR), High Resolution (HR) and Medium Resolution (MR).
- Level 2
  - This product contains the information about the Ocean Swell Spectra (OSW). Also included in this level is the Surface Radial Velocity (RVL).

A detailed overview on the different offerings can be found in Fig. 2.6.

2.2.4 Radar Backscattering at different surfaces

The radar backscattering is influenced in a complex manner by a variety of factors, which can be grouped into two main categories: sensor parameters and surface parameters.

Sensor parameters

- Wavelength
  - The Sentinel-1 C-band sensor works with a frequency of 5.405 GHz. This corresponds to a wavelength of 5.54 cm (Table 2.1)
- Incidence angle
  - Signals emitted from different orbits will have different incidence angle for a particular point on Earth, thus obtaining different backscattering results as shown in Fig. 2.7. In Interferometric Wide Swath mode, the incidence angle ranges between 29.1° - 46.0° (Table 2.2).
- Polarisation
  - The SAR sensor transmits a longitudinal eletromagnetic wave. It is possible to transmit the longitudinal wave in a single plane (polarisation). It is also possible for the SAR sensor to select the polarisation of the received signal (Fig. 2.8). Usually, most scatterers reflect the wave in the same polarisation (co-polarised: HH, VV). However, some of the signal may come back in a different plane, cross-polarised: HV and VH [17]. For the regions in Switzerland analysed in this thesis, Sentinel-1 in IW mode provides VV and VH polarisations. The main applications of each polarisation are shown as follows:
    * VV polarisation , has applications in studying the small-scale roughness of (capillary) waves on the water surface, thus it is used extensively for surface wind speed extraction.
    * HH polarisation is important in the study of soil moisture, due to it's capacity to penenetrate vertically oriented crops (e.g. wheat and barley). Also, HH is very suitable for separating marine ice and water, since it is less sensitive to water roughness than VV polarisation, thus producing an improved contrast between the two target types. For a similar reason, HH is used for ship detection.
    * Cross-polarised SAR (VH or VH) detection from water surfaces is very low. For this reason, it's suitable for detecting targets on the water surface, as well as

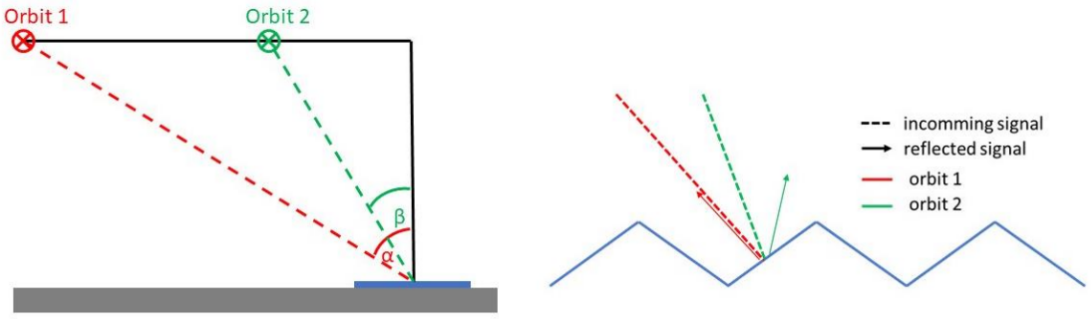

Figure 2.7: Orbits with different incident angle on the same point on Earth [2].

ice deformations (ridging, fractures, and rubble). Additionally, in the case of forestry, the use of cross polarisation will improve the forest/non-forest discrimination and the retrieval of low biomass values (forest regeneration, regrowth, plantation).

Surface parameters

Surface parameters which can be either geometrical factors such as roughness, landscape topography, etc. or physical factors such as the permittivity of the material on the surface (Table 2.3). Significant factors for lakes are also wind speed and direction, and the water content in snow. For smooth and plain water, almost all radiation is scattered away from the sensor making it appear very dark. As the wind speed picks up, waves occur on the water surface and significant scattering can occur. When perfectly plain water is covered by perfectly plain ice, microwaves penetrate the ice without absorption and are reflected at the ice-water interface, however, away from the sensor and the ice covered lake appears to be completely black, at least in theory. In reality, cracks in the ice scatter some microwaves back to the sensor. Therefore, visible and well located cracks are clear indicators for ice cover. Furthermore, in reality, the ice-water interface is never completely smooth, therefore some scattering can occur at these boundaries which, however, can be weak. The older the ice, the more air bubbles are enclosed in the ice which increase the backscatter within the ice volume by direct backscattering and also by double reflection of microwaves at the air-bubbles and the ice-water interface. With snow cover, the air-ice interface becomes increasingly rough which further increases the backscatter signal. Finally, with snow melt, the liquid water content of the overlying snow pack increases which significantly reduces the backscatter signal as the ice-water mixture of wet snow absorbs a significant fraction of the microwave energy [18].

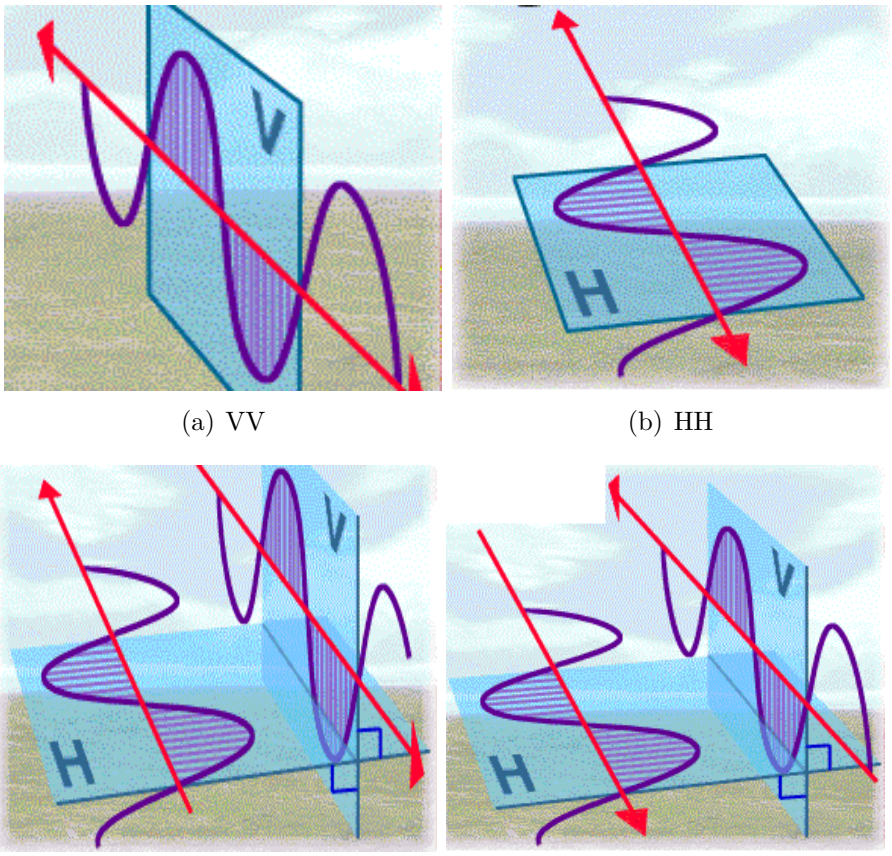

(a) VV (b) HH

(c) VH (d) HV

Figure 2.8: Polarisations in different planes

Table 2.3: Estimated relative permittivity in Farads per meter (F/m) for different materials [5].

Material	Estimated relative permittivity
Soft new snow	4
Dry sand or rock	8
Granular snow	15
Compact wet snow	50
Pure water	80
Pure ice	95

Table 2.4: Sentinel-2 MSI: MultiSpectral Instrument, Level-1C. Resolution is given in meters (m), Wavelenght in nanometers (nm)

Name	Resolution (m)	Wavelenght (nm)	Description
B1	60	443.9 (S2A) / 442.3 (S2B)	Aerosols
B2	10	496.6 (S2A) / 492.1 (S2B)	Blue
B3	10	560 (S2A) / 559 (S2B)	Green
B4	10	664.5 (S2A) / 665 (S2B)	Red
B5	10	703.9 (S2A) / 703.8 (S2B)	Red Edge 1
B6	20	740.2 (S2A) / 739.1 (S2B)	Red Edge 2
B7	20	782.5 (S2A) / 779.7 (S2B)	Red Edge 3
B8	10	835.1 (S2A) / 833 (S2B)	NIR
B8A	20	864.8 (S2A) / 864 (S2B)	Red Edge 4
B9	60	945 (S2A) / 943.2 (S2B)	Water vapor
B10	60	1373.5 (S2A) / 1376.9 (S2B)	Cirrus
B11	20	1613.7 (S2A) / 1610.4 (S2B)	SWIR 1
B12	20	2202.4 (S2A) / 2185.7 (S2B)	SWIR 2
QA60	60		Cloud mask

2.3 Multispectral Instrument

2.3.1 ESA SENTINEL-2 data products

All is this section is taken from [19] if nothing else is stated.

There are 3 main processing steps in the Sentinel 2 pipeline, Level-0, Level-1 (A,B, and C) and Level-2 (A). Following we described the characteristics of the only 2 products available to users: Level-1C and Level-2A.

- Level 1C
  - It includes radiometric and geometric corrections including ortho-rectification and spatial registration on a global reference system with sub-pixel accuracy. It results into a **Top of Atmosphere (TOA)** product with 13 UINT16 spectral bands representing TOA reflectance scaled by 10000. Bands with their corresponding name, resolution, wavelenght, and description are listed in Table 2.4.
- Level 2A
  - It includes a scene classification and an atmospheric correction applied to TOA products. Level-2A main output is an orthoimage **Bottom of Atmosphere (BOA)** corrected reflectance product in Table 2.4.

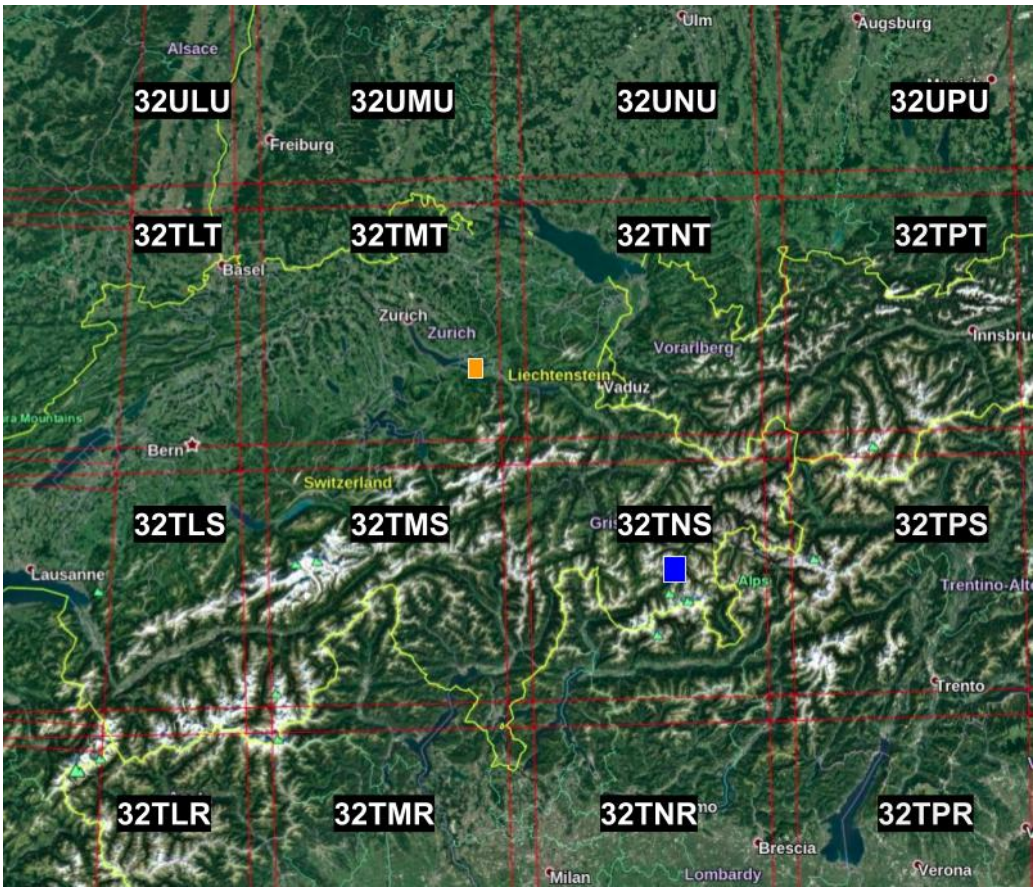

Figure 2.9: Sentinel 2 tiles in UTM/WGS84 projection. Lake Sihl (shown as purple filled rectangle) in corresponds to 32TMT, and lakes in Region Sils shown as yellow filled rectangle) correspond to 32TNS.

2.3.2 Tiles

All is this section is taken from [20] if nothing else is stated. For Level-1C and Level-2A, the granules, also called tiles, are 100x100km2 ortho-images in UTM/WGS84 projection. The UTM (Universal Transverse Mercator) system divides the Earth's surface into 60 zones. Each UTM zone has a vertical width of 6° of longitude and horizontal width of 8° of latitude. In Fig. 2.9 are shown the tiles corresponding to the Swiss territory.

2.4 Google Earth Engine

Google Earth Engine (GEE) is a planetary-scale platform for Earth science data & analysis. It stores and provides datasets from Earth Observation satellite missions, preprocesses them, and makes them freely accessible for education and research. GEE consists of a web-based application for visualisation and with capacity to perform analysis work including classifications using machine learning algorithms like SVM, Random Forests, or K Means, with limited

computational capacity [21]. For further in-depth analysis, it is possible to run data collection operations in order to download data via Google Drive, which provides GeoTiff and TFRecord formats. Among the imagery catalogs available in GEE are Sentinel, Landsat, and MODIS. Following are described the preprocessing steps performed by GEE to provide Sentinel 1 and 2 imagery.

2.4.1 Sentinel-1 SAR GRD

For Sentinel-1 the image set is called COPERNICUS/S1_GRD. This dataset contains Level-1 Ground Range Detected (GRD) images which are preprocessed from Google and provide backscatter coefficients in decibels. Google Earth Engine provides for Sentinel-1 data the following five preprocessing steps with the Sentinel-1 Toolbox from ESA [21]:

- Apply orbit file
  - Changes the orbit file with a corrected orbit file
- GRD border noise removal
  - Corrects the noise at the border of the images
- Thermal noise removal
  - Corrects the thermal noise between the sub-swaths
- Radiometric calibration
  - Calculates the backscatter intensity using the GRD metadata
- Terrain correction
  - Corrects the side looking effects using the SRTM 30 meters digital elevation model

The thermal noise removal, radiometric calibration and terrain correction are explained in more detail in the following subsections.

2.4.2 Thermal noise reduction

This chapter is based on [22]. Thermal noise in satellite radar data originates mostly from the heat generated by the satellite itself. It can become a problem if the backscattered radar signal is of low intensity (dark image) and this noise has to be removed to give reliable information. There are two different thermal noise corrections applicable.

- Empirical thermal noise removal
- Theoretical thermal noise removal

An empirical thermal noise correction is based on the assumption that highly reflective target areas, for example water surfaces without any disturbances, are not sending back any radar signals. Noise signals in these areas are then considered thermal noise and are deducted from the whole image. The advantage of this procedure is that it is very easy and produces comparable results. On the other hand, in most cases there are only a few suitable target areas available and in the end it remains empirically with a lot of uncertainties. In contrast, a theoretical noise correction is using the whole set of metadata from the radar images. The advantage of this procedure is, that any image can be used. The results of this correction are also comparable with other images, which are corrected with this method. The theoretical correction is based on Eq. 2.1:

$$N_\sigma = n_r * log(\frac{r_s}{r}) - 2 * G_r + 10 * log(sin(I))) \tag{2.1}$$

- n_r = noise reference level
- r_s = slant range
- r = reference angle
- G_r = antenna pattern correction
- I = incidence angle

A theoretical thermal noise reduction has been applied by Google Earth Engine to all data used in this thesis. It is stated that the preprocessing tools of the Sentinel-1 Toolbox from ESA have been used.

2.4.3 Radiometric calibration

This chapter is based on [23]. The radiometric calibration transforms the radar reflectivity to physical units (for example decibel). The radar reflectivity contains a real and an imaginary part. The Level 1 products of Sentinel 1 contain Calibration Annotation Data Sets (CADS). Four Look Up Tables (LUT) can be found in these datasets. With one of them it is possible to transform the radar reflectivity A_σ into the radar cross-section σ^0 . After this correction the area is normalized and is aligned with the ground range plane. In the CADS an average height

is used on an ellipsoid earth model. With this ellipsoid at hand, the area normalization factor can be simplified to $sin(\alpha)$ for the radar cross-section. Eq. 2.2 is needed for the calculation of the radar cross-section σ^0:

$$\sigma^0 = \frac{DN^2 * K}{A_{dn}^2} * \frac{1}{G_{eap}^2} * (\frac{1}{R_{ref}})^3 * sin(\alpha) \tag{2.2}$$

- $\frac{1}{G_{eap}^2}$ = elevation antenna pattern (EPA) correction
- $(\frac{1}{R_{ref}})^3$ = range spreding loss (RSL) correction
- A_{dn} = product final scaling from internal SLC to final SLC or GRD
- α = local incidence angle of the used earth model
- K = calibration constant
- DN = pixel amplitude directly taken from the measurement file

In the case of Sentinel-1, the EAP and RSL corrections are by default applied by the S-1 IPF such that the above formula simplifies to Eq. 2.4.3:

$$\sigma^0 = \frac{DN^2}{A_{dn}^2 * K} * sin(\alpha) \tag{2.3}$$

If the Look up Tables (LUT) are used Eq. can be simplifeyd to the Eq. :

$$\sigma^0 = \frac{DN^2}{A_{\sigma}^2} \tag{2.4}$$

A radiometric calibration has been applied by Google Earth Engine to all data used in this thesis. It is stated that the preprocessing tools of the Sentinel-1 Toolbox from ESA have been used.

2.4.4 Terrain correction

The following section is based on [24]. The terrain correction removes distortion effects originating from the side looking geometry of the radar system. This is necessary because otherwise the radar images could not be used in combination with other georeferenced products as for example a shapefile. A short summary about three important distortion effects due to the side looking geometry of a SAR are listed below:

- Slant-range scale distortion:

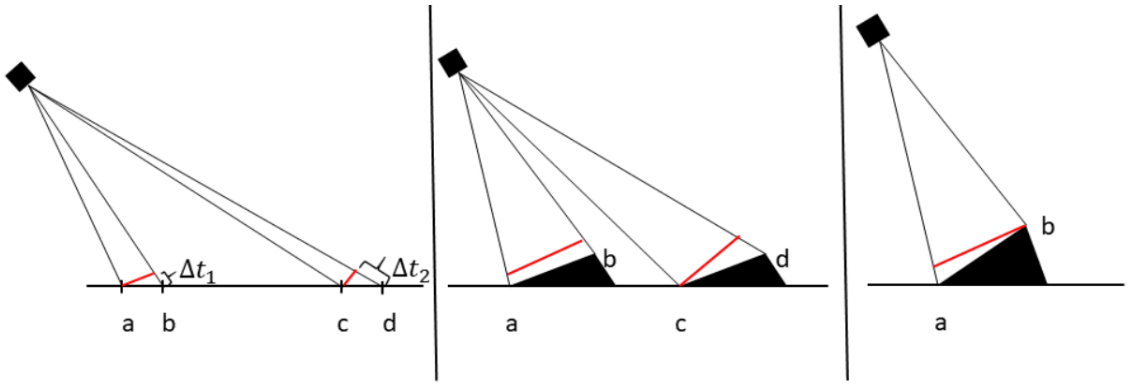

Figure 2.10: Left: Slant range scale distortion, middle: Foreshortening, right: Layover

  - This effect is visualized in Fig. 2.10 at the left. The distances on the ground between $a-b$ and $c-d$ have the same length. However, in the radar image the distance $c-d$ will be longer than the distance $a-b$. The reason is that radar measures distances over time differences. The red lines in Fig. 2.10 are symbolizing the front of a radar wave, Δt_1 is smaller than Δt_2 . That means that the distance for the radar wave traveling to $a-b$ will be shorter and the wave will be reflected earlier at the surface leading to a shorter total time between transmitting and receiving the radar wave package, resulting in a shorter ab distance.

- Relief displacement:

  - **Foreshortening:** this effect is caused by the surface of the earth. In Fig. 2.10 in the middle the effect is visualized. The distance $a-b$ on the slope of the mountain will be measured as zero. The radar wave will be reflected at a and b at exactly the same time. If the slope of the mountain is not parallel to the radar wave front (as visualized between c and d, the distance will be measured as too short because of the slant-range distortion (see point above).
  - **Layover:** In a layover the radar wave front hits the top of the mountain first. The radar reflection at the top of the mountain will be reflected before the signal reaches the ground of the mountain. This means as shown in Fig. 2.10 at the right, that for point b, the horizontal distance to the satellite is shorter than the horizontal distance of point a. In the radar image the slope of the mountain lays above the bottom (point a) of the mountain.

All data used in this thesis have been terrain corrected by the algorithms of Google Earth Engine. It is stated that the preprocessing steps of the Sentinel-1 Toolbox from ESA have been used.

2.5 Introduction to Machine Learning Models

2.5.1 Support Vector Machine (SVM)

Support Vector Machine is currently a hot topic in the statistical learning area. In late 1990s, the traditional neural network approaches suffered severe difficulties with generalization and producing models which is the main reason for the foundation of Support Vector Machines. In statistical learning, support vector machines are supervised learning method with associated leaning algorithms that analyse dataset [25].
In a $p-dimensional$ space, a *hyperplane* is a flat affine subspace (a subspace need not pass through the origin) of dimension $p-1$. It is defined by equation

$$\beta_0 + \beta_1 x_1 + ... + \beta_p x_p = 0 \tag{2.5}$$

for parameters $\beta_1 ... \beta_p$, in this case the point $X = (x_1 ... x_p$ lies on the hyperplane. Now, suppose X does not satisfy 2.5, but

$$\beta_0 + \beta_1 x_1 + ... + \beta_p x_p > 0 \tag{2.6}$$

then we say X lies on the one side of the hyperplane. On the other hand, if

$$\beta_0 + \beta_1 x_1 + ... + \beta_p x_p < 0 \tag{2.7}$$

then X lies on the other side of the hyperplane.

Based on this, we can demostrate that the hyperplane is able to divides this $p-dimensional$ space into two halves, which will be the basic idea of classification.

In order to decide which separating hyperplane to use, we need to use the maximal margin classifier, which is also known as the optimal separating hyperplane (Fig. 2.11). The maximal margin classifier is farthest from the training observation. That is, when we compute the distance of each observation to the separating hyperplane, the minimal one is what we called *the margin*. The maximal margin classifier is the hyperplane for which the margin is the largest [26].

2.5.2 Convolutional Neural Networks

Neural Networks consist of individual units called neurons that are grouped by layers. When images are fed to such an architecture, the computer sees it as an array of pixels and tries to

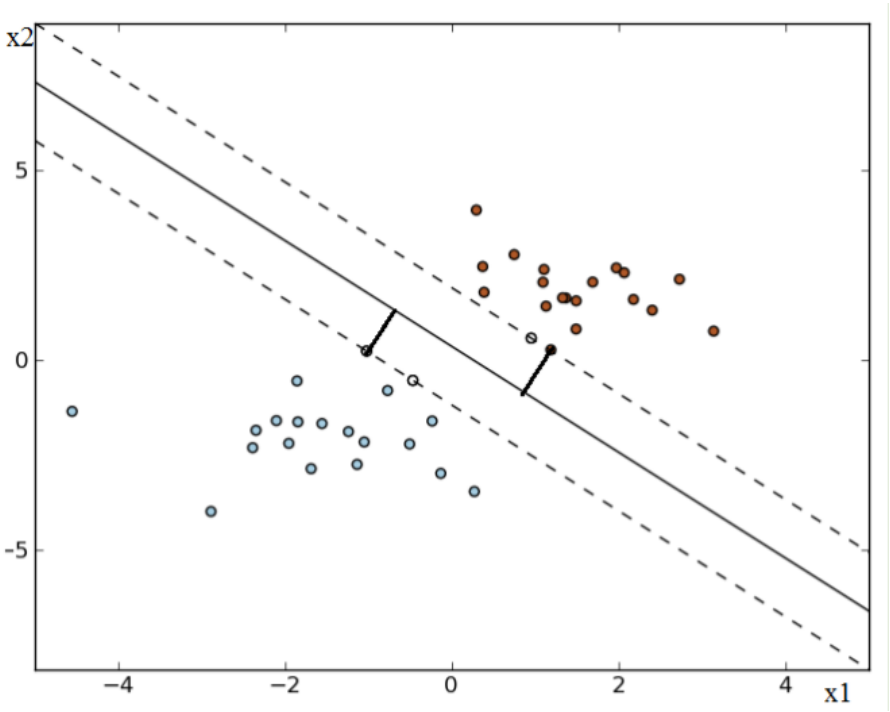

Figure 2.11: SVM hyperplane in a binary classification.

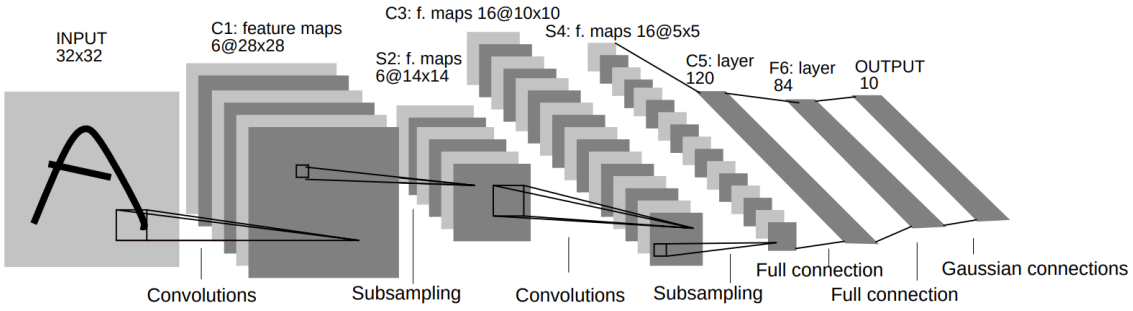

Figure 2.12: Example of the structure of Convolutional Neural Network [3]

look for a base pattern, some kind of features that can lead the image to a specific image-level label, pixel-level label or instance level label. In a supervised scenario, the dataset comprises of images and labels which are fed into the network together. Figure 2.12 shows one of the first CNN based Image classification models called LeNet [3].

Generally, a convolution is defined as an operation between two real-valued functions, each function usually represents, for example, a signal or measurement. This operation is applied in a form of a filter, also called a kernel, across the input image in a sliding window fashion. These filter weights are parameters that are learned with back-propagation. Their convolutional layers are mostly combined with pooling layers to prevent the network from growing indefinitely and helps the network to generalize better. Pooling layers are very popular with image classification networks where the output nodes are equal to the number of classes. But, these are not very efficient with image segmentation tasks where spatial information is

of utmost priority [27]. A further description about the network in use for this thesis and its parameters is shown in chapter 5.

2.5.3 Semantic Segmentation

Semantic segmentation refers to the process of linking each pixel in an image or a region of interest (lake in our case) to a class label 2.13. The standard semantic segmentation model works on the concept of encoder-decoder architecture, which converts the image into a compact form, like a latent space, and then this form is decoded to get pixel-level information. The dimensionality of this latent space is much lower than that of the original image space. And, this gives rise to the concept of downsampling and upsampling [27].

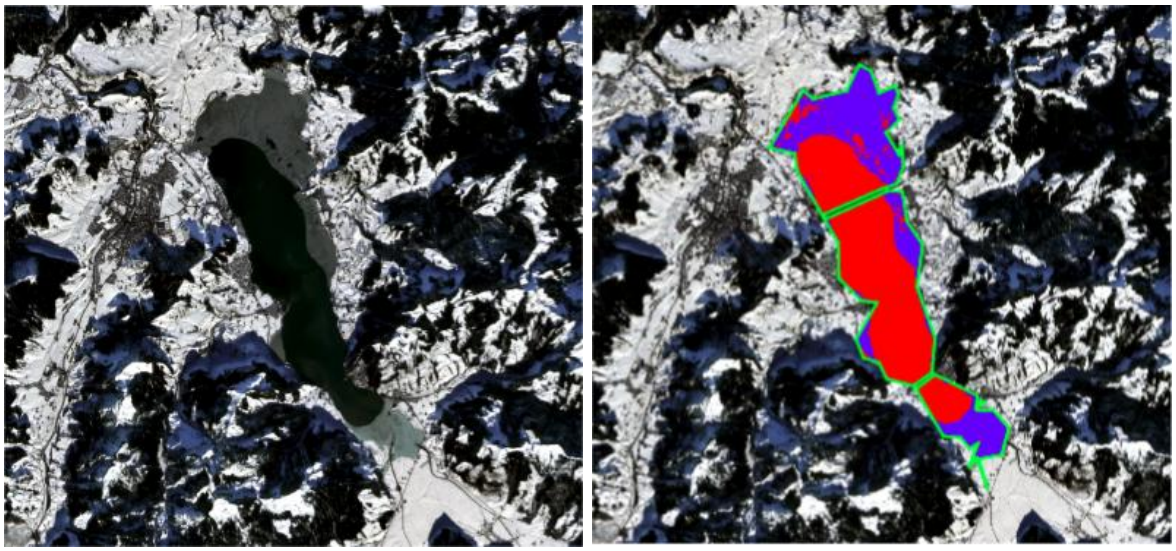

(a) RGB image (b) Pixel-wise classification

Figure 2.13: Semantic Segmentation of the lake Sihl (Red: non-frozen, Blue: frozen) on top of a RGB image from Sentinel 2, on a transition day from non-frozen to frozen (31/12/2017).

Downsampling and Upsampling. One of the fundamental methods to downsample an image is regular pooling. Pooling layers reduce the dimensionality of the input space along with keeping the information of the significant features intact like highlighting the max features. Another method which can serve the same purpose as pooling is strided convolutions. The benefit of using convolutional striding over pooling is that pooling operation is fixed but convolutions can be learned. In other words, we are trying to learn the "pooling operation" thereby increasing the models expressive ability. For upsampling, the goal is to increase the spatial resolution so that the final output vector (semantic label) has the same dimension as the input vector space. For that, strided transpose convolutions come into the picture. These functions go from deep and narrow layers to wider and shallower ones [27].

Fully Convolutional Neural Networks. The first end-to-end trainable fully convolutional network for image segmentation was devised by [28]. The network is fully convolutional and uses deconvolutional layers to upsample the feature maps back to the original input size. This is trained using pixel-wise loss. Moreover, this model employs skip connections to combine high-level feature map representations with more specific and dense ones at the top of the network.

Transfer learning. Deep supervised classification approaches need huge amount of labelled data and a large amount of resources to train a model from scratch. Such data volumes are often not available. Even if they are, labelling them is costly and increases the computational cost of model training. *Transfer learning* mitigates this bottleneck by using an already trained model from some related task as a starting point. Given the fact that the initial layers of a neural network learn rather generic local image properties, a model trained on a huge image dataset can be re-utilized on a different dataset with a much smaller amount of fine-tuning (re-training) to the specific characteristics of the new data [18].

Chapter 3

Related work

Many studies discussed the trends in lake ice formation in different parts of the globe. For example, trends in lake freeze-up and break-up across Canada for a long period from 1951 until 2000 [29], decreasing tendency in lake freezing in several Swiss lakes were reported in [7]. Later, response and role of ice cover in lake-climate interactions was reviewed [30]. This paper observed that the ability to accurately monitor lake ice will be an important step in the improvement of global circulation models, regional and global climate models and numerical weather forecasting. Canadian Lake Ice Model (CLIMo) is used to simulate lake ice phenology across the North American Arctic from 1961-2100 [31], using two climate scenarios produced by the Canadian Regional Climate Model (CRCM). They projected changes to the ice cover using 30-year mean data between 1961-1990 and 2041-2070, which suggested a probable drift in freeze-up (0-15 days later) and break-up (10-25 days earlier). For lakes, that work reviewed a number of topics, including ice cover concentration, ice extent and phenology, and ice types, as well as ice thickness, snow on ice, snow/ice surface temperature, and grounded and floating ice cover on shallow Arctic and sub-Arctic lakes.

Using Radar data. It was proposed to determine the depth and thickness of ice in shallow lakes and ponds using the Landsat Thematic Mapper and European Remote Sensing (ERS)-1 SAR data [32]. Almost a decade later, a study of the shallow lakes in the north slope of Alaska to find the response of ice cover on the climate conditions using Radar remote-sensing and numerical analysis was done [33]. A machine learning-based automated ice-vs-water classification was proposed using dual polarisation SAR imagery [34]. Later, A study on the ice freezing and thawing detection in shallow lakes from Northern Alaska with spaceborne SAR imagery was performed [35]. Ice phenology in lakes of the Lena river delta was monitored using TerraSAR-X backscatter [36]. An assessment of lake ice phenology in the Northern Hemisphere from 2002 to 2015 was performed [37]. The effect of the lake size on the accuracy of a threshold-based classification of ground-fast and floating lake ice from Sentinel-1 SAR data was assessed [38]. Recently, an interesting machine learning approach was put forward to detect wet and dry snow in mountainous areas using Sentinel-1 SAR data [39]. Moreover ,various algorithms such

as thresholding, Iterative Region Growing with Semantics (IRGS) and k-means were presented for the generation of a floating lake ice product from Sentinel-1 SAR data for various permafrost regions (Alaska, Canada and Russia) [40]. RADARSAT-2 SAR data has been used to monitor ice cover in lakes during the spring melt period in the Yukon area of the Canadian Arctic [41]. They put forward a threshold-based classification methodology and observed that the HH and HV backscatter from the lake ice have significant temporal variability and inter-lake diversity, RADARSAT-2 imagery was used to develop a threshold-based method to determine lake phenology events for the mid-latitude lakes in Central Ontario from 2008 to 2017 [42]. Also, RADARSAT-2 imagery (dual polarised) was used for developing a lake ice classification system acquired over lake Erie, with the IRGS method [43]. Additionally, polarimetric RADARSAT-2 (C-Band) was used to observe the scattering mechanisms of bubbled freshwater lake ice [44].

SAR data analysis is challenging, and deep learning could play a significant role because of its ability to learn task-specific, hierarchical image features. [45] used CNNs to estimate sea ice concentration using SAR data acquired during freeze-up period in the Gulf of St. Lawrence on the east coast of Canada. Deep Learning was used to detect ice on Swiss lakes using SAR Sentinel-1 data, based on a pixel-wise classification with 2 classes, *frozen* and *non-frozen* [18].

Using webcams. A system that detects lake ice in webcam data with the help of a deep neural network is described in [8]. Public webcams have two main advantages compared to optical satellite images. Firstly, they are usually not affected by clouds, except for the comparatively rare case of dense fog. Secondly, they have a very high temporal resolution (up to one image per 10 min). Though the approach generated excellent results, it also has disadvantages. Webcams are usually placed arbitrarily (e.g., too far away or covering a small lake area), and often only low above the lake, leading to great scale differences between front and back of the lake surface. Moreover, they are prone to hardware failure, and, being very cheap cameras, they have poor spectral and radiometric quality with significant compression artifacts. Another practical problem with webcams is that it is very difficult to operationalise them at country- or even world-scale. Finally, deep learning based system, capable to classify per pixel water, ice, and snow on crowd-sourced images was implemented [46].

Using optical data. A machine learning-based methodology for lake ice detection using low resolution optical satellite images was proposed [6]. The main problem with optical satellite images is the data loss due to clouds. However, the authors showed that the algorithm produces consistent results when tested on data from multiple winters. In addition, researchers used Landsat-8 multi-spectral data for extraction of frozen lakes and water-vs-ice classification [47]. Recently, a feasibility study, which targeted for a unified lake ice monitoring system that combines images from optical satellites, in-situ temperature data and webcam images [48].

Chapter 4

Data

4.1 Sentinel-1

Sentinel-1 maps the same point on Earth several times within one repeat cycle. Due to the large across-track area coverage of the satellites and the latitude of our target area in Switzerland (and most other areas where lakes freeze), the revisit time is further reduced. For the lakes in study, it can bee seen from Table 4.3 that the temporal resolution in winter $2017-18$ is better than that of $2016-17$. This is because of missing data from *S1B*. Though *S1B* was launched in April 2016, the corresponding data is fully available in the GEE platform (refer Section 4.2, data collection and pre-processing) only from March 2017. In addition, Sentinel-1 scans the lakes in Region Sils with four orbits and lake Sihl is scanned by two (Table 4.2).

Table 4.1: Dataset statistics for Sentinel 1 and Sentinel 2, shown as (S1 / S2). The non-transition days, on which a lake is fully frozen or fully non-frozen, and transition days (partially frozen dates) are shown. For S1 all available observations are available in the table, for Sentinel 2, only observations with cloudiness less than 30% per lake. *acq.* denotes the number of acquisitions along the winter, *lake pixels* the number of pixels corresponding to each lake per observation.

Lake	**Winter**	**Non-transition days**		**Transition days**	**Total**	**# lake**
		Non-frozen	**Frozen**		**# acq.**	**pixels**
Sihl	2016-17	44 / 20	14 / 4	3 / 1	61 / 25	104927
	2017-18	61 / 13	10 / 1	19 / 4	90 / 18	
Sils	2016-17	40 / 9	42 / 5	37 / 1	119 / 15	40908
	2017-18	76 / 9	65 / 6	40 / 5	181 / 20	
Silvaplana	2016-17	36 / 7	44 / 4	39 / 2	119 / 13	26563
	2017-18	85 / 9	66 / 5	30 / 5	181 / 19	
St. Moritz	2016-17	66 / 6	42 / 5	11 / 1	119 / 12	7521
	2017-18	84 / 9	77 / 5	20 / 4	181 / 18	

For lake Sihl and region Sils, Sentinel-1 operates in IW mode (refer to Section 2.2.2 for more details on mode and polarisation) polarises the emitted and detected signals only in *VV* and *VH* modes as shown in Fig. 2.4. The distribution of backscatter values of *frozen* and *non-frozen* pixels in these bands are shown in Fig. 4.2. Note that the separability in *VV* appears better than in *VH*.

Table 4.2: Details of the orbits scanning *Region Sils* (lakes Sils, Silvaplana, St. Moritz) and lake Sihl, such as orbit number, flight direction, scan start time in Universal Coordinate Time (UTC), and approximate incidence angle.

	Orbit	Flight dir.	Scan time	Incidence angle
Region Sils	15	ascending	17:15	41.0°
	66	descending	05:35	32.3°
	117	ascending	17:06	30.8°
	168	descending	05:26	41.7°

	Orbit	Flight dir.	Scan time	Incidence angle
Sihl	15	ascending	17:15	41.0°
	66	descending	05:35	32.3°

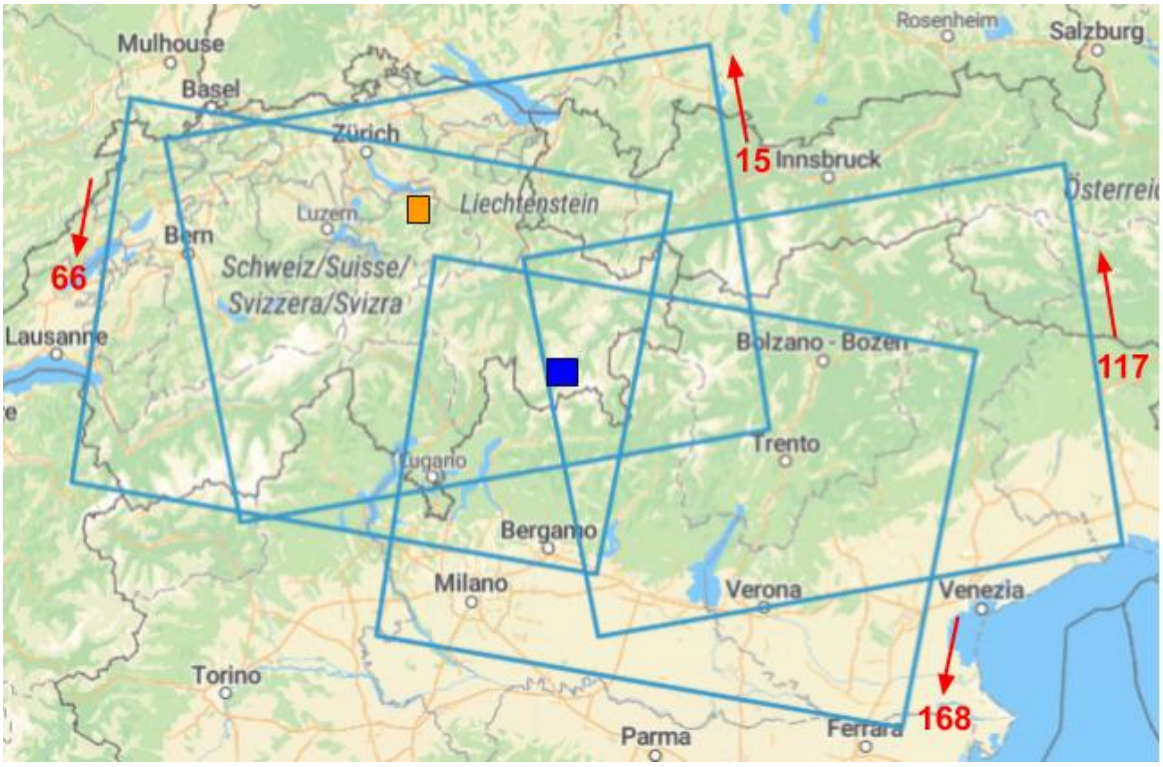

Figure 4.1: Location of the two regions of study with their corresponding Sentinel-1 orbits and directions (*ascending* or *descending*). Lake Sihl shown in yellow, Region Sils shown in blue. Flight paths were obtained from [4].

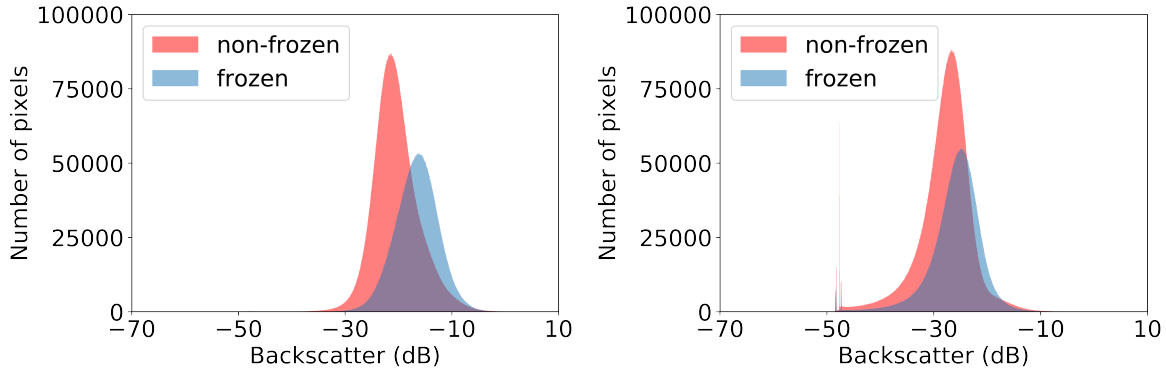

(a) Distribution of VV

(b) Distribution of VH

Figure 4.2: Distribution of frozen and non-frozen pixels for VV and VH polarisations (combined data from lakes Sihl, Sils, Silvaplana and St. Moritz along 2 winters).

4.2 Sentinel-2.

Table 4.3: Temporal resolution of different sensors and an integrated system. *S1* contains all SAR images, *S2 (clear only)* contains the count of the images with cloudiness $< 70\%$, S1+S2 contains the count of *S1 + S2 (clear only)*, and *S1 + S2 (all images)* contains the count *S1+S2*. When combining both *S1* and *S2*, the intersection of both sensors on the same day in counted just as 1.

Lake	**Winter**	S1	S2 (clear only)	S1+S2	S1+S2 (all images)
Sihl	2016-17	4.5	10.92	3.9	2.81
	2017-18	3.0	15.2	2.87	2.28
Sils	2016-17	2.3	18.2	2.14	1.96
	2017-18	1.5	13.7	1.47	1.37
Silvaplana	2016-17	2.3	22.75	2.1	1.96
	2017-18	1.5	14.4	1.47	1.37
St. Moritz	2016-17	2.3	22.75	1.95	1.96
	2017-18	1.5	15.2	1.44	1.37

Data collection and pre-processing. *Google Earth Engine (GEE)* is a cloud-based platform for large-scale geo-spatial data analysis [21]. It stores and provides data of various satellite missions, performs data pre-processing and makes them freely available for education and research purposes. The Sentinel-1 backscatter coefficients (in decibels) were downloaded from the GEE platform after several inbuilt pre-processing steps such as GRD *border noise removal* which corrects the noise at the border of the images, *thermal noise removal* for correcting the thermal noise between the sub-swaths, *radiometric calibration* which calculates the backscatter intensity using the GRD metadata, *terrain correction* to correct the side looking effects using the digital elevation model (SRTM, 30m), and *log-scaling* to transform the approximate distribution of the SAR responses from *Chi-squared* to *Gaussian* (see Fig. 4.2). We note that we did not perform any absolute geolocation correction, since the back-projected lake

outlines suggested a sufficient accuracy.

Transition and non-transition days. All the data from two winters was divided into two categories: *non-transition* dates where the lake is fully frozen or fully non-frozen, and *transition* dates with partially frozen lake surface. Both the freeze-up and break-up dates belong to the transition category. The dataset statistics are shown in Table 4.3.

Ground truth. For each lake, a single label (*frozen, non-frozen*) per day was assigned by a human operator after visual interpretation of the freely available webcam data. The webcam-based ground truth thus generated was further enriched by visual interpretation of the Sentinel-2 images whenever available. However, some remaining noise in the ground truth is likely due to interpretation errors, as a result of overly oblique viewing angles of webcams and compression artefacts in the images. Note also, we have the ground truth available only for the non-transition days.

After back-projecting the digitised lake outlines from Open Street Map (OSM) on to the SAR images, for each lake, we extract the the *lake pixels* which lie inside the polygon derived from the lake outline. The only lake which required additional processing was *Sihl*, since it contains 2 bridges which were remove, leaving only clean pixels in the shape.

Chapter 5

Methodology

5.1 Sentinel 1

Semantic Segmentation. We define lake ice detection as a two class (*frozen, non-frozen*) pixel-wise classification problem and tackle it with the state-of-the-art semantic segmentation network *Deeplab v3+* [9]. The *non-frozen* class comprises of only *water* pixels. Whereas a pixel is considered to be part of the *frozen* class if it is either *ice* or *snow*, since in the target region, the frozen lakes are covered by snow for much of the winter. The standard procedures in machine learning-based data analysis are followed. The dataset is first divided into mutually exclusive *training*, *validation* and *test* sets. The *Deeplab v3+* model is then fitted on the training set. This model is further used to predict the images in the validation set, which provides an unbiased evaluation of the model's predictive performance outside the training set while tuning the hyper-parameters. Lastly, the trained model is tested on the previously unseen test dataset.

Deeplab v3+ is a deep neural network for semantic segmentation [9], which has set the state-of-the-art in multiple semantic segmentation benchmarks, including among others PASCAL VOC 2012 [49] and Cityscapes [50]. It combines the advantages of both Atrous Spatial Pyramid Pooling (ASPP) and encoder-decoder structure. Atrous convolution allows one to explicitly control the resolution of the features computed by the convolutional feature extractor. Moreover, it adjusts the field-of-view of the filters in order to capture multi-scale information. *Deeplab v3+* also incorporates depthwise separable convolution (per-channel 2D convolution followed by pointwise 1×1 convolution) which significantly reduces the model size. The architecture of *Deeplab v3+* is shown in Fig. 5.1.

Network parameters. We used the *mobilenetv2* implementation of *Deeplab v3+*, as available in *TensorFlow*. The *train crop size* was set to 129×129 (effective patch size is 128×128) and the *eval crop size* to the full image resolution. All models were trained for $40'000$ iterations with a batch size of 8. Atrous rates were set to $[1, 2, 3]$ for all experiments. The cross-entropy loss function was minimised with standard stochastic gradient descent, with a base learning rate of $1e - 3$.

Transfer learning. We use a *Deeplab v3+* model pre-trained on the PASCAL VOC

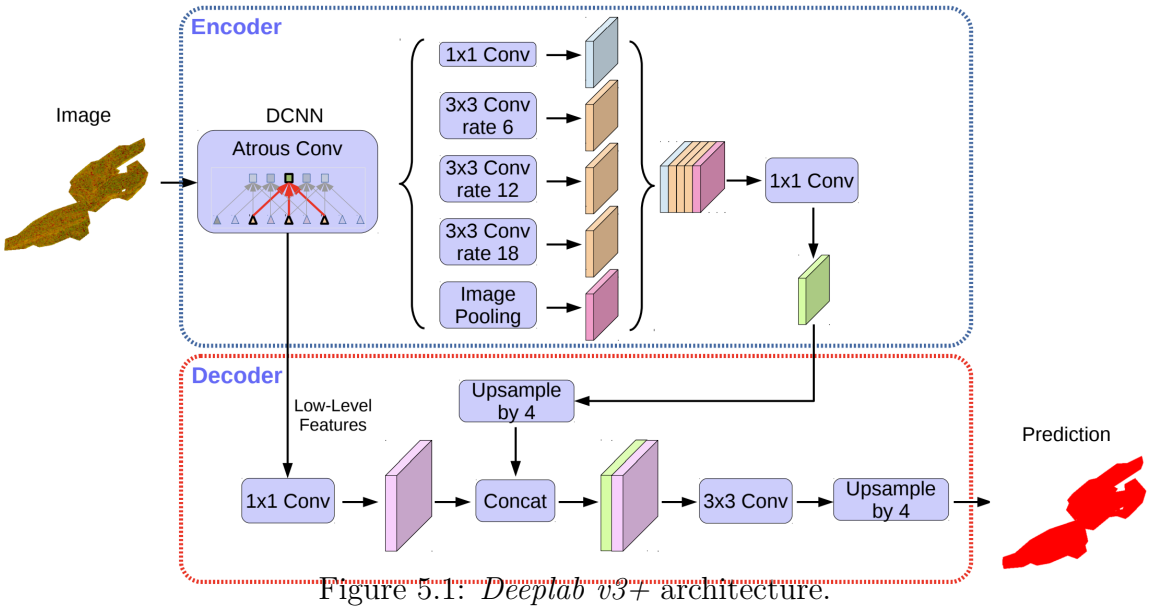

Figure 5.1: *Deeplab v3+* architecture.

2012 close-range dataset as the starting point and fine-tune it on the relatively small Sentinel-1 SAR dataset (see Table 4.3). Surprisingly, we find that pre-training on RGB amateur images greatly improves the performance even on a data source as different as interferometric Radar, with greatly improved results compared to training from scratch only on the SAR data.

5.2 Sentinel 2

SVM. A sklearn implementation [51] was used to perform a pixel-wise classification from Sentinel-2 images, this with a *linear kernel*, regularization parameter (C) set to 1.0, *gamma* set to scale, and *tolerance* set to $1e$-3. Only non-cloudy pixels were taking into account, masking cloudy pixel with the Sentinel-2 cloud mask product. For training a balance dataset is created, the smaller class with n pixels is completely taken, and from the other class only n pixels are randomly selected.

5.3 Sentinel 1+2 System

Multi-temporal analysis First, a daily prediction in percentage of non-frozen pixels is performed. Then, a time series is created, with values from Sentinel 1 and 2, if for the same day data from both sensors is available, then Sentinel 2 result is chosen. After that, a median filter with K=3 is applied on top of the result.

Ice on/off. The ice on and ice off identify when the freezing up and breaking up processes occur, respectively. The ice on occurs after 2 consecutive days with percentage of non-frozen pixels $> 90\%$. In the other hand, the ice off dates occurs after 2 consecutive days have a percentage of non-frozen pixels $< 90\%$.

Chapter 6

Experiments & Results

We use various measures to quantify performance, including recall, precision, overall accuracy, and the IoU score (Jaccard index). In semantic segmentation experiments, we used only *lake pixels* and only non-transition dates to train the network and to compute performance metrics. This is due to the lack of per-pixel ground truth on the transition dates. However, qualitative analysis and time series analysis are done on all the dates.

6.1 Quantitative results

For developing an ideal operational system for lake ice monitoring, the data from a couple of lakes from a few winters would have to be used to train the model which can then be tested on unseen lakes and winters. However, generating ground truth for each lake is a tedious task. Nevertheless, we make sure that the data from at least one lake from one full winter is in the training set for the classifier to learn the proper class decision boundaries.

We employ Cross-Validation (CV), i.e., the data is partitioned into k folds, usually of approximately the same size. Then, the evaluation is done k times, each time using one fold as test set and the union of all remaining folds as training set. *Leave-one-out cross-validation* is the setting where the number of folds equals the number of instances (in our case the number of winters/lakes) in the dataset.

6.1.1 Leave one-winter out CV

The goal of *leave-one-winter-out CV* is to investigate the generalisation capability of a model trained on one winter when tested on a different winter. The results for Sentinel-1 are shown on Table 6.1 and for Sentinel-2 on Table. For Sentinel-1, it can be seen that we achieve excellent results for both winters with average accuracies of 93.1% and 93.8% for $2016-17$ and $2017-18$ respectively. Sentinel-2 average accuracies are 96.5% and 81.6% as shown in Fig. 6.3. The results show that the proposed model generalises well across the potential domain shift caused by the specific conditions of different winters, without having seen data from any day

Table 6.1: Leave one winter out cross validation on Sentinel-1. Top: Results on 2016-17, trained on 2017-18, Bottom: Results on 2017-18, trained on 2016-17. Total units are in millions of pixels, except for precision, recall, and **accuracy** (bottom right cell in each table).

True \ Prediction	Non-frozen	Frozen	**Recall**
Non-frozen	8.58	0.05	99.4%
Frozen	0.87	3.84	81.6%
Precision	90.8%	98.8%	**93.1%**

True \ Prediction	Non-frozen	Frozen	**Recall**
Non-frozen	12.4	0.25	98.0%
Frozen	0.88	5.09	85.3%
Precision	93.2%	95.4%	**93.8%**

Table 6.2: Per-class- and mean IoU values of frozen and non-frozen classes for each lake. Sentinel-1 data of a lake from winter $2016-17$ is tested using a model trained on the data lakes from all lakes in $2017-18$.

IoU \ Winter	2016-17	2017-18
Non-frozen	90.7%	91.5%
Frozen	81.9%	81.9%
Mean	86.3%	86.7%

within the test period. See Tables 6.2 and 6.4 for the per-class and mean IoU values for each winter.

Table 6.3: Leave one winter out cross validation on Sentinel-2. Top: Results on 2016-17, trained on 2017-18, Bottom: Results on 2017-18, trained on 2016-17, with a balanced dataset (number of -non-frozen pixels is equal to the number of frozen pixels). Total units are in millions of pixels, except for precision, recall, and **accuracy** (bottom right cell in each table).

Prediction / True	Non-frozen	Frozen	**Recall**
Non-frozen	2.61	0.02	99.4%
Frozen	0.11	0.76	98.0%
Precision	96.1%	98.0%	**96.5%**

Prediction / True	Non-frozen	Frozen	**Recall**
Non-frozen	1.59	0.40	80.0%
Frozen	0.06	0.45	88.1%
Precision	96.3%	53.0%	**81.6%**

Table 6.4: Per-class- and mean IoU values of frozen and non-frozen classes for each lake. Sentinel-2 data of a lake from winter $2016-17$ is tested using a model trained on the data lakes from all lakes in $2017-18$, with a balanced dataset (number of -non-frozen pixels is equal to the number of frozen pixels).

Winter / IoU	2016-17	2017-18
Non-frozen	95.5%	77.6%
Frozen	86.1%	49.5%
Mean	90.8%	63.6%

6.1.2 Leave one-lake out CV

We also report results of a *leave-one-lake-out* CV experiment to check the generalisation capacity of the model across lakes. The results are shown on Tables 6.5 and 6.7. While testing for all data of a lake (e.g. *Sils*) from two winters, the data from the other two lakes (e.g. *Sihl, Silvaplana, St. Moritz*) from the same two winters is used for training. The prediction achieves >84.9% overall accuracy for all four lakes. As a side result of this experiment, we also report the precision-recall curves in Fig. 6.1 for a detailed per-class performance assessment. For both the frozen and non-frozen classes, the area under the curve is nearly optimal for lake Sils and very good performance is achieved on lakes Silvaplana and St. Moritz, for Sihl, a lake located in a completely different region from the rest of the lakes and with half temporal resolution results were significantly lower in both sensors. See Tables 6.6 and 6.8 for the per-class and mean IoU values for each lake on Sentinel-1 and Sentinel-2 respectevely.

The mean IoU for lake Sihl on winter is significantly lower than the other leave one-winter out experiments, also it makes the leave one-winter out decrease its accuracy. As shown in Table A.13, IoU for class *frozen* is below 35% for every individual training set. One of the reasons that explain this situation are the *non-frozen* days in which the *cloud mask* is not marking those pixels as clouds (27/09/2017 and 30/04/2018), and the SVM algorithm is classifying them as *frozen*. Also, a *frozen* (32/12/2017) is classified mostly as *non-frozen*, since is an "black" icy day, and due to the lack of these samples in other training sets, most of pixels are misclassified.

Table 6.5: Results on **Sentinel-1** for lakes Sihl, Sils, Silvaplana, and St. Moritz. Confusion matrices are shown for the **leave-one-lake-out** cross-validation experiment. Units are in millions of pixels, except for precision, recall, and **accuracy** (bottom right cell in each table).

Sihl

Prediction / True	Non-frozen	Frozen	**Recall**
Non-frozen	9.15	1.82	83.4%
Frozen	0.22	2.29	91.4%
Precision	97.7%	55.7%	**84.9%**

Sils

Prediction / True	Non-frozen	Frozen	**Recall**
Non-frozen	5.22	0.01	99.9%
Frozen	0.39	4.01	91.1%
Precision	93.0%	99.9%	**95.9%**

Silvaplana

Prediction / True	Non-frozen	Frozen	**Recall**
Non-frozen	3.61	0.02	99.4%
Frozen	0.22	2.67	92.4%
Precision	94.2%	99.3%	**96.3%**

St. Moritz

Prediction / True	Non-frozen	Frozen	**Recall**
Non-frozen	1.05	0.05	95.3%
Frozen	0.08	0.79	90.7%
Precision	92.8%	93.8%	**93.2%**

Table 6.6: Per-class and **mean IoU** values of frozen and non-frozen classes for each lake. **Sentinel-1** data of a lake from winter $2016 - 17$ is tested using a model trained on the data lakes from all lakes in $2017 - 18$.

IoU / Lake	Sihl	Sils	Silvaplana	St. Moritz
Non-frozen	81.8%	92.9%	93.8%	88.7%
Frozen	52.9%	91.0%	91.8%	85.5%
Mean	67.3%	92.0%	92.8%	87.1%

Table 6.7: Results on **Sentinel-2** for lakes Sihl, Sils, Silvaplana, and St. Moritz. Confusion matrices are shown for the **leave-one-lake-out** cross-validation experiment. Units are in millions of pixels, except for precision, recall, and **accuracy** (bottom right cell in each table).

Sihl

True \ Prediction	Non-frozen	Frozen	**Recall**
Non-frozen	3.12	0.28	91.7%
Frozen	0.07	0.56	88.2%
Precision	97.7%	66.2%	**91.1%**

Sils

True \ Prediction	Non-frozen	Frozen	**Recall**
Non-frozen	0.65	0.04	94.2%
Frozen	0.04	0.39	91.3%
Precision	94.5%	90.8%	**93.1%**

Silvaplana

True \ Prediction	Non-frozen	Frozen	**Recall**
Non-frozen	0.39	0.01	98.2%
Frozen	0.03	0.21	89.3%
Precision	94.0%	96.7%	**94.9%**

St. Moritz

True \ Prediction	Non-frozen	Frozen	**Recall**
Non-frozen	0.11	0.00	98.3%
Frozen	0.02	0.06	74.9%
Precision	85.7%	96.7%	**89.1%**

Table 6.8: Per-class and **mean IoU** values of frozen and non-frozen classes for each lake. **Sentinel-2** data of a lake from winter $2016 - 17$ is tested using a model trained on the data lakes from all lakes in $2017 - 18$.

IoU \ Lake	Sihl	Sils	Silvaplana	St. Moritz
Non-frozen	89.7%	89.4%	92.4%	84.5%
Frozen	60.8%	83.6%	86.7%	73.1%
Mean	75.3%	86.5%	89.5%	78.8%

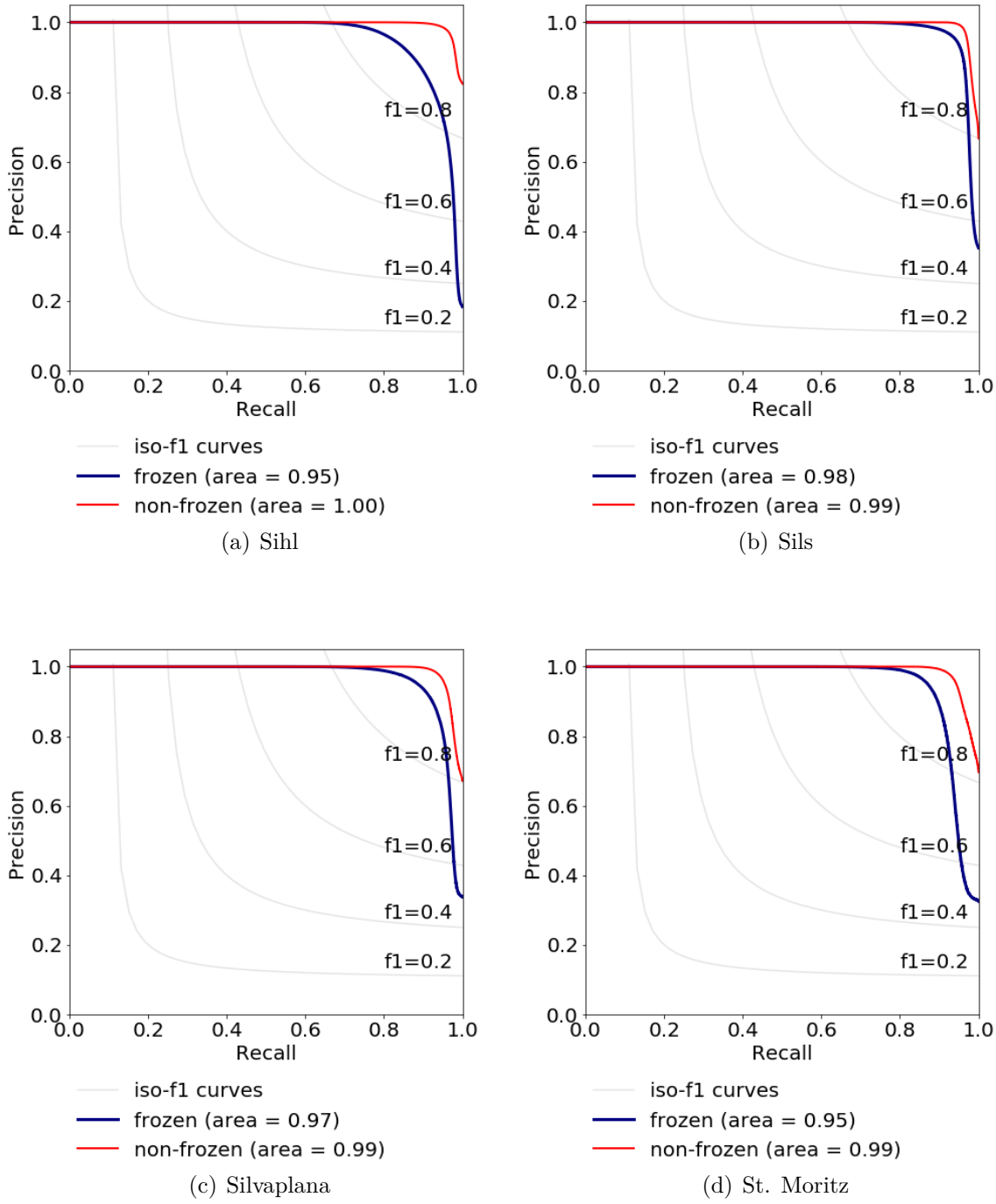

(a) Sihl (b) Sils

(c) Silvaplana (d) St. Moritz

Figure 6.1: Precision-recall curves for lakes Sihl, Sils, Silvaplana, and St. Moritz. The *iso-f*1 curve connects all points in the precision/recall space whose $F1$ scores are the same. Sentinel-1 data of a lake from two winters ($2016-17$ and $2017-18$) forms the test set for a model trained on the data from the other two lakes in both winters.

6.2 Qualitative analysis.

Exemplary qualitative results are depicted in Fig. 6.2. We show the classification results on frozen, non-frozen, and transition dates along with the probability map (blue means higher probability of frozen, red means higher probability of non-frozen). For better interpretation of the result, especially for the transition date, we show the corresponding image from Sentinel-2.

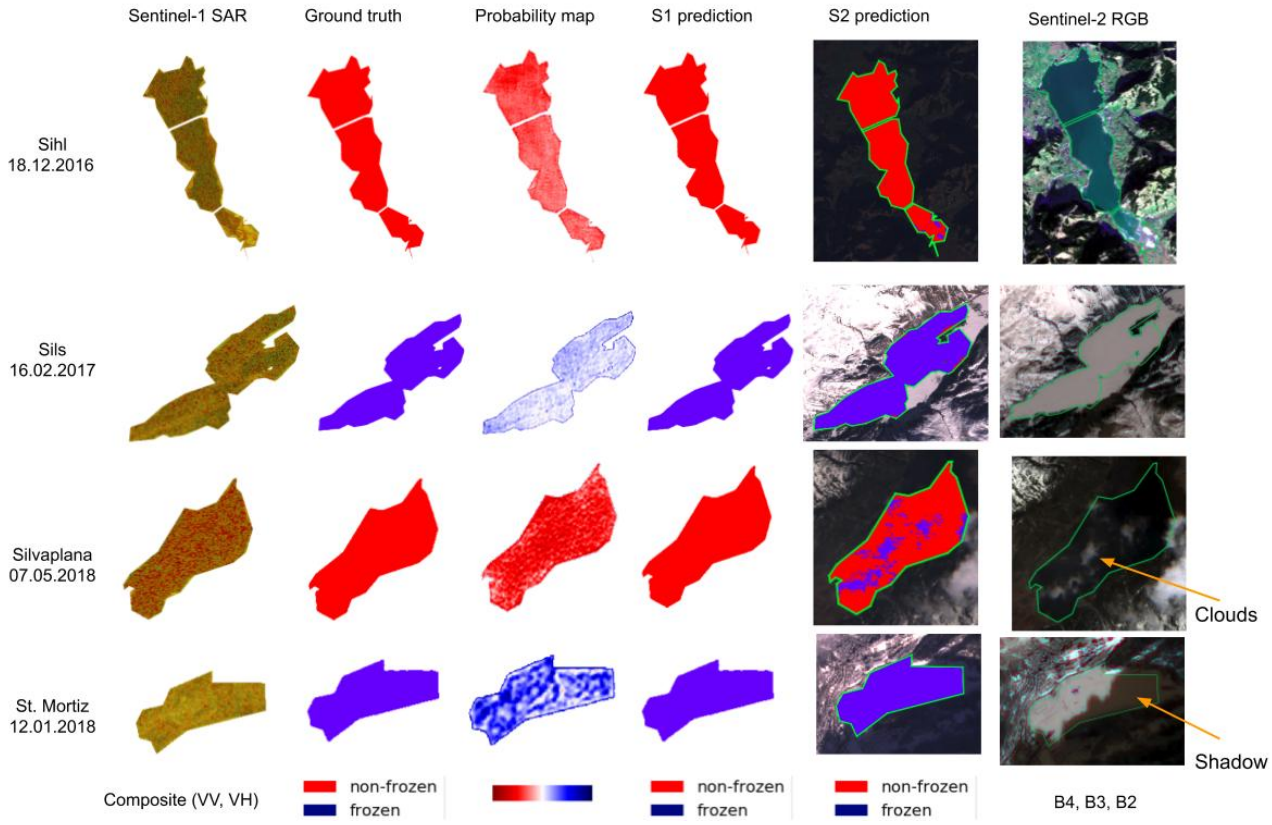

Figure 6.2: Qualitative results for lake Sihl on a non-frozen day (row 1), lake Sils on a frozen day (row 2), and lake Silvaplana on a non-frozen day with clouds (row 3), and lake St. Moritz on a frozen day with a shadow on top. For each lake we show the Sentinel-1 composite image (column 1), the ground truth (column 2), the predicted probability map from Deeplab (column 3), and the corresponding binary classification map (column 4). Additionally, column 5 shows the corresponding prediction from SVM, and in column 6 Sentinel-2 image for better visual interpretation.

Discriminating between snow/ice and water should be particularly difficult in case of strong wind and associated waves, due to the increased roughness of the water. We have checked for correlations with the wind speed (available from nearby weather stations), but could not find any clear relationship. It appears that the system can handle windy conditions practically equally well – which is further supported by the excellent overall results, as the area is moderately wind-prone such that repeated failures on windy days would impact the overall statistics. Clouds don't represent any issue for SAR, but for optical data, even when we don't

take into account pixels that are masked out due to cloudiness the problem is not completely solved, since the cloud mask presents some true negatives that are directly treated by the SVM as frozen, as shown in Silvaplana case in Fig. 6.2.

6.3 Time-series.

The *ice-on* and *ice-off* dates are of particular interest for climate monitoring. From the per-day semantic segmentation results, we estimate the daily percentage of frozen surface for each observed lake. Thus, for each available SAR image, we compute the percentage of frozen pixels, throughout the entire winter. Although we do not have per-pixel ground truth on the partially frozen transition days, we know whether the lake has more water (shown with a value of 75% in the ground truth) or more ice/snow (shown with a value of 25% in the ground truth). Even though some miss-classifications exist during the transition days, the non-transition days are almost always predicted correctly, probably because the network was trained entirely on non-transition days. In Figures 6.3, 6.4, 6.5, 6.6, 6.7, 6.8 are shown the results of percentage of frozen pixels and for a comparison, we also plot the time series of the temperature values (sliding window mean of the daily median, window size of 7 days) obtained from the nearest meteo station. The corresponding detection of *ice on* and *ice off* days is detailed in Table 6.9, where the ground truth of the event, the detection by only using *Sentinel-1* and by combining *Sentinel-1* and *Sentinel-2* is calculated for the first occurrence *freeze up* of *break up* per lake, per winter.

Table 6.9: Dataset statistics. The non-transition days, on which a lake is fully frozen or fully non-frozen, and transition days (partially frozen dates) are shown. S1 contains results per day from Sentinel-1, with a median filter with K=3. S1+S2 contains results per day combining Sentinel-1 and Sentinel-2, with a median filter with K=3. Highligheted in green are shown the predictions with ±3 days from the ground truth (GT).

Lake	**Winter**	**Ice on**			**Ice off**		
		GT	**S1**	**S1+S2**	**GT**	**S1**	**S1+S2**
Sihl	2016-17	01.01	23.01	11.01	14.03	04.03	04.03
	2017-18	27.12	30.12	30.12	06.01	05.01	01.01
Sils	2016-17	03.01	10.01	10.01	13.04	16.04	16.04
	2017-18	02.01	25.12	20.12	09.04	31.03	30.03
Silvaplana	2016-17	04.01	18.01	18.01	15.04	27.01	19.03
	2017-18	02.01	29.12	29.12	09.01	22.01	22.01
St. Moritz	2016-17	16.12	29.12	15.01	01.04	03.01	30.03
	2017-18	22.12	23.12	23.12	26.04	13.03	13.03

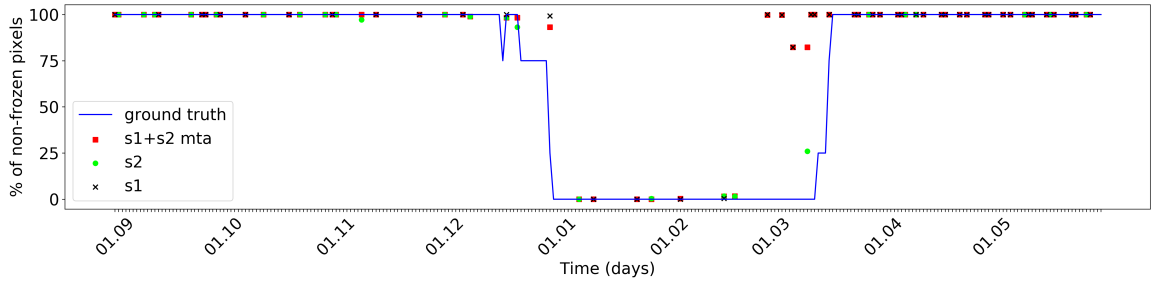

(a) Time series of percentage of non-frozen pixels for lake Sihl from winter 2016 – 17.

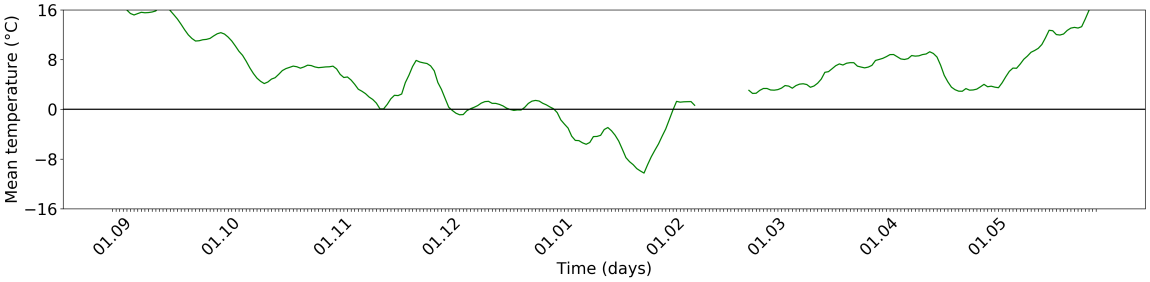

(b) Temperature (temporal moving average with window size of 7 days) from the nearest meteo station (Einsiedln).

Figure 6.3: Correlation of our results (winter 2016 – 17) on lake Sihl with the ground truth and the auxiliary temperature data.

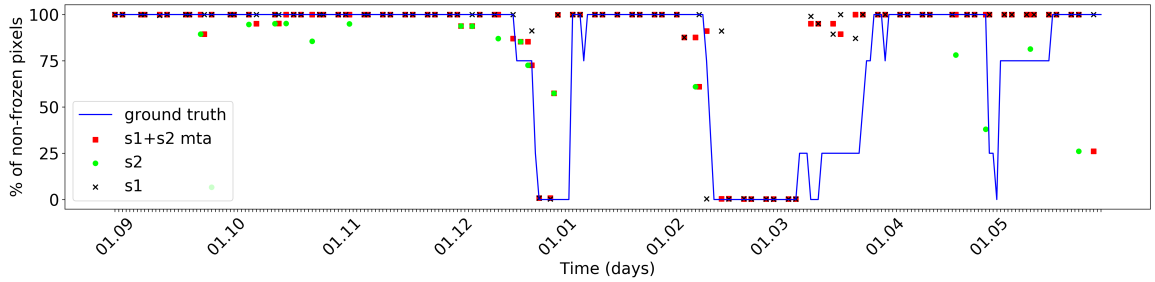

(a) Time series of percentage of non-frozen pixels for lake Sihl from winter 2017 – 18.

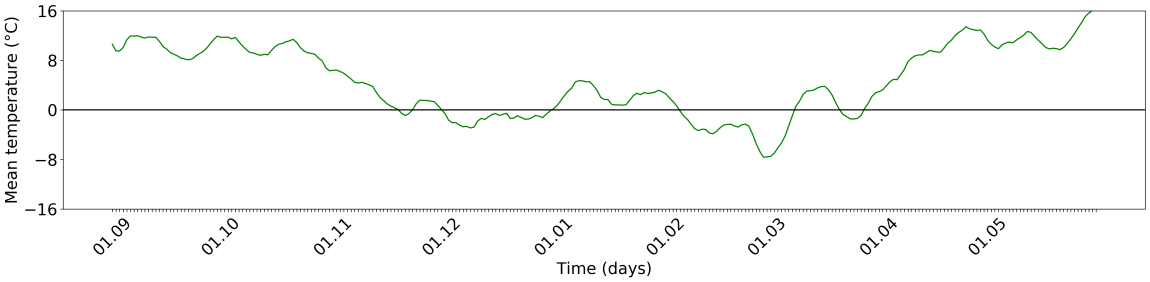

(b) Temperature (temporal moving average with window size of 7 days) from the nearest meteo station (Einsiedln).

Figure 6.4: Correlation of our results (winter 2017 – 18) on lake Sihl with the ground truth and the auxiliary temperature data.

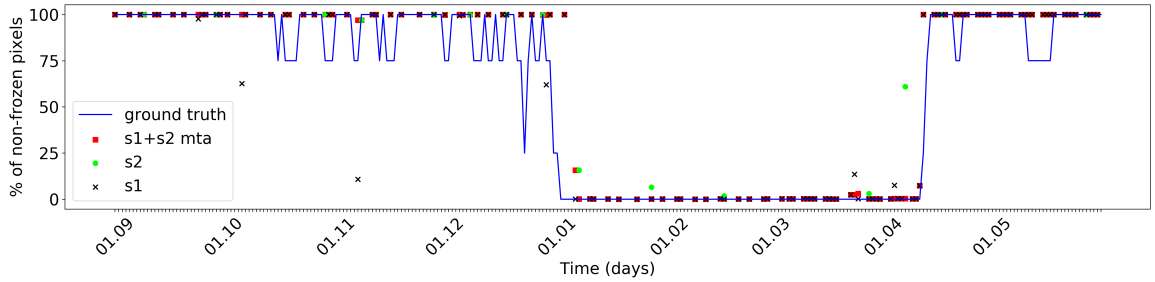

(a) Time series of percentage of non-frozen pixels for lake Sils from winter $2016-17$.

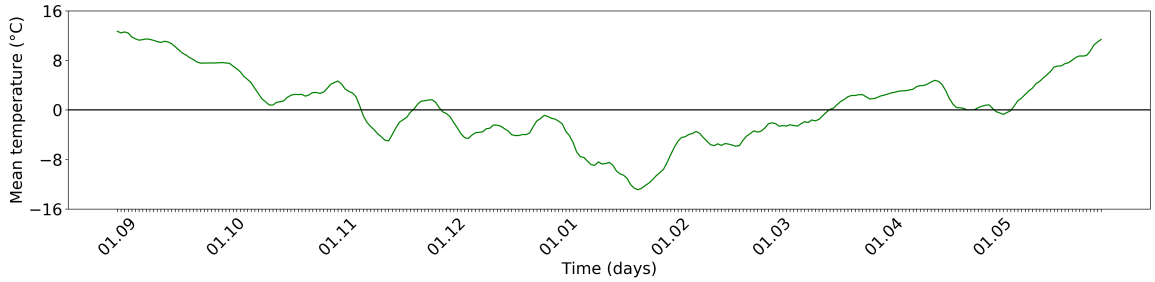

(b) Temperature (temporal moving average with window size of 7 days) from the nearest meteo station (Segl Maria).

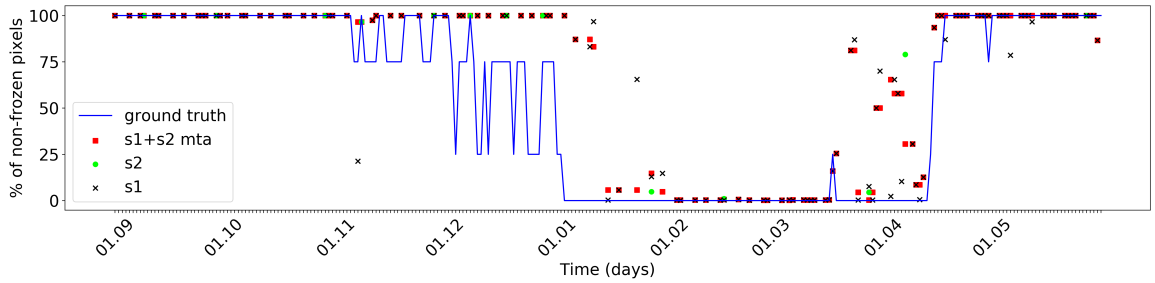

(c) Time series of percentage of non-frozen pixels for lake Silvaplana from winter $2016-17$.

Figure 6.5: Correlation of our results (winter $2016-17$) on lake Sils with the ground truth and the auxiliary temperature data.

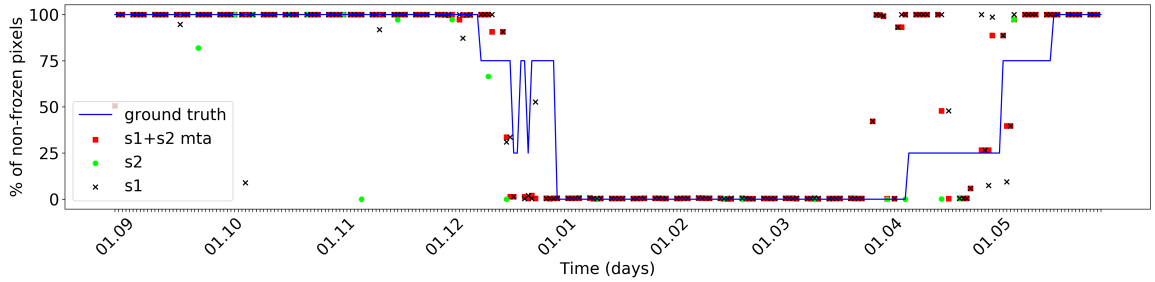

(a) Time series of percentage of non-frozen pixels for lake Sils from winter $2017-18$.

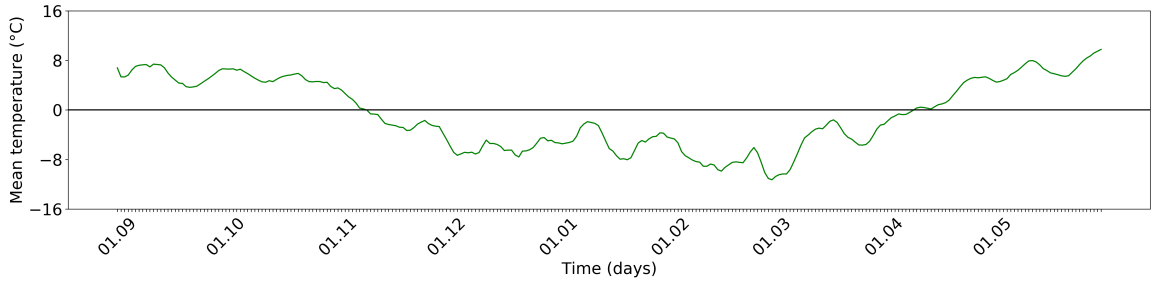

(b) Temperature (temporal moving average with window size of 7 days) from the nearest meteo station (Segl Maria).

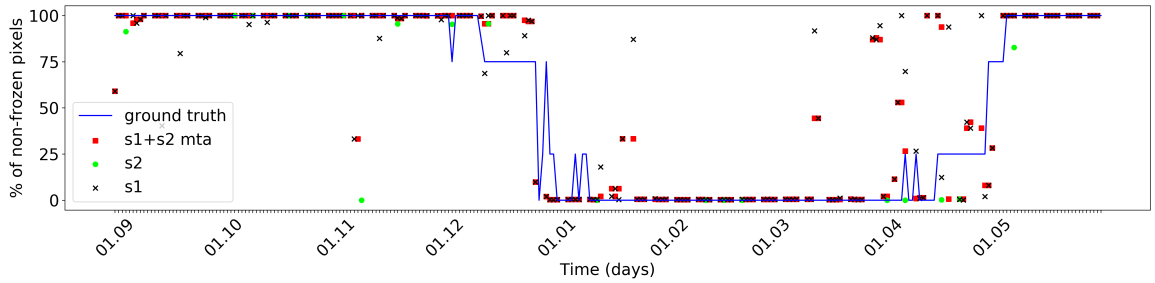

(c) Time series of percentage of non-frozen pixels for lake Silvaplana from winter $2017-18$.

Figure 6.6: Correlation of our results (winter $2017-18$) on lake Sils with the ground truth and the auxiliary temperature data.

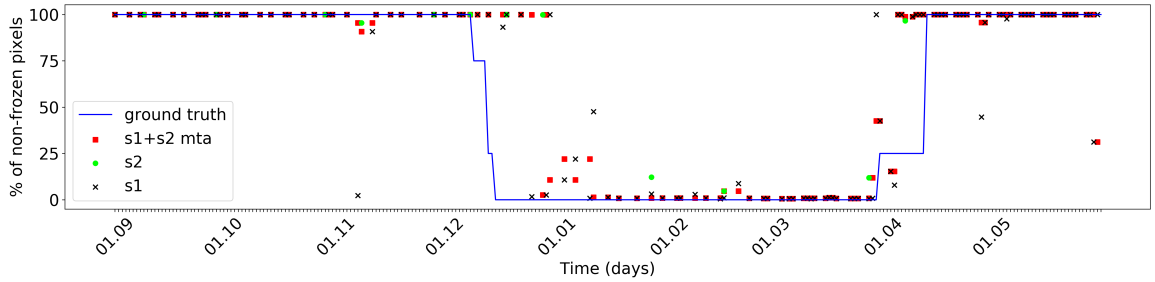

(a) Time series of percentage of non-frozen pixels for lake St. Moritz from winter 2016 – 17.

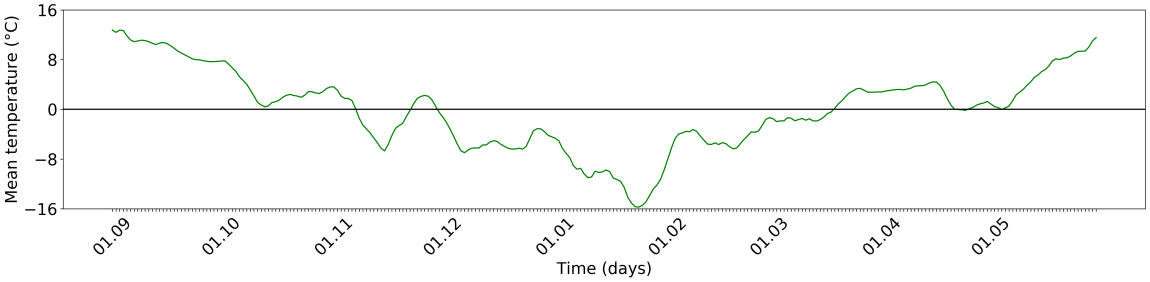

(b) Temperature (temporal moving average with window size of 7 days) from the nearest meteo station (Samedan).

Figure 6.7: Correlation of our results (winter 2016 – 17) on lake St. Moritz with the ground truth and the auxiliary temperature data.

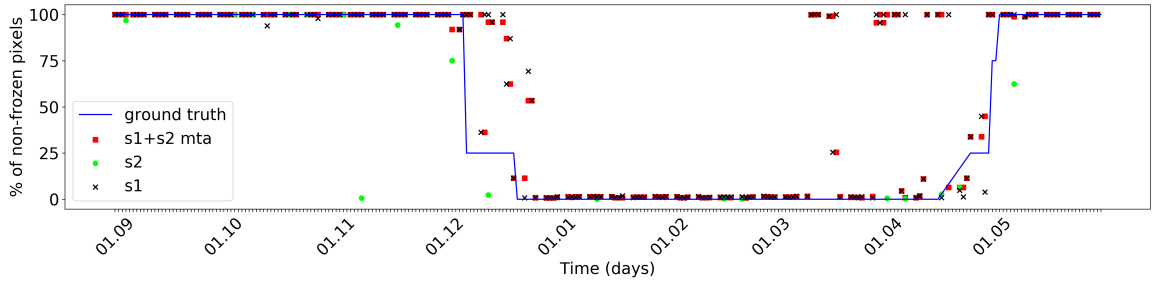

(a) Time series of percentage of non-frozen pixels for lake St. Moritz from winter 2017 – 18.

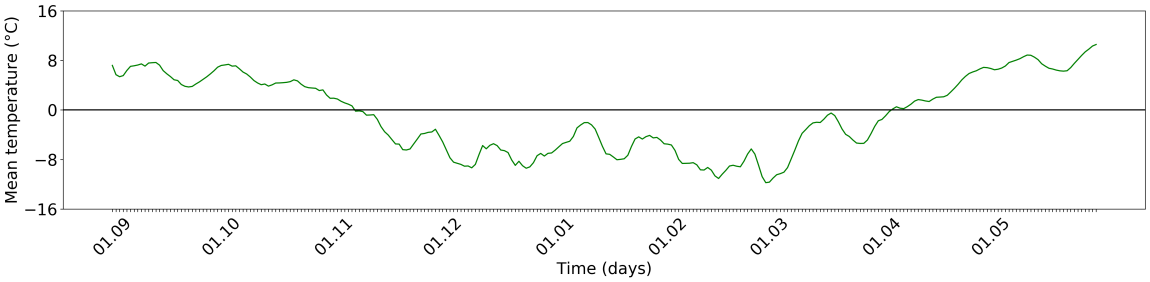

(b) Temperature (temporal moving average with window size of 7 days) from the nearest meteo station (Samedan).

Figure 6.8: Correlation of our results (winter 2017 – 18) on lake St. Moritz with the ground truth and the auxiliary temperature data.

6.4 Miscellaneous experiments SAR

In all the experiments reported so far, we used the data from all four orbits (both ascending and descending) and both polarisations (VV and VH). To study the individual effect of polarisations VV and VH, we drop either of them and report the corresponding results on Table A.24 (left). Note that mIoU drops by almost 33.1% when VV is left out, while it drops by only 3% without VH, confirming the significance of polarisation VV for lake ice detection. This finding is also aligned with the visual differences in Fig. 4.2. Note that we used the data from all four orbits in this experiment.

Table 6.10: Per-class- and mean IoU values of frozen and non-frozen classes with different polarisations. Data from all the four lakes from winter $2016-17$ was tested using a model trained on the data from all four lakes from winter $2017-18$.

Polarisation / IoU	VV, VH	VH	VV
Non-frozen	90.4%	75.2%	88.6%
Frozen	80.8%	39.7%	76.7%
Mean	85.6%	57.5%	82.6%

Chapter 7

Conclusions and Outlook

We have described a system for reliable monitoring of lake ice based on Sentinel-1 SAR and Sentinel-2 multispectral imagery, with the potential to retrieve long, consistent time series over many years (assuming continuity of the satellite mission). The proposed method has been demonstrated for four different Swiss lakes over two complete winters, and obtains good results (accuracy higher than 84%), even when generalising to an unseen winter or lake. Given the main advantage of SAR data for our purposes its ability to observe with very good spatial and temporal resolution independent of clouds we see the possibility to extend our method into an operational monitoring system. A logical next step would be to process longer time series, which unfortunately is not yet possible with Sentinel-1. It is quite possible that even a moderate time span, say 20 years, would suffice to reveal trends in lake freezing patterns and perhaps also correlations with climate change. When combining Sentinel-1 with an optical sensors, in our case Sentinel-2, the temporal resolution increases, however it's not enough to make significant improvements in the ice on/off detection compared to Sentinel-1 only. For this reason, A combination of Sentinel-1 with a low spatial high temporal resolution optical satellite (e.g. MODIS , VIIRS) might bring improvements. Also, adding webcam for detection of exact dates of freeze up and break up, could ensure reliable identification of *ice-on* and *ice-off* dates within the GCOS specification of ± 2 days. Lake location-wise, our system is generalizing well across lakes in the same region, where the incidence angle, temporal resolution, altitude, and wind conditions are similar. However, when a lake with different characteristics appears, the current system is capable to achieve an *overall accuracy* $> 80\%$, but not a mean IoU $> 80\%$.

Bibliography

[1] "Esa sentinel user guides - sentinal-1 mode, polarisation, and observation geometry." `https://sentinel.esa.int/web/sentinel/missions/sentinel-1/observation-scenario`. Retrieved 2020-12-05.

[2] P. Imhof, "Deep-learning-based lake ice detection using esa sentinel-1 sar data," 2019.

[3] Y. LeCun, L. Bottou, T. Bengio, and P. Haffner, "Gradient based learning applied to document recognition," *Proceedments of the IEEE*, 2019.

[4] "Alaska satellite facility." `search.asf.alaska.edu`. Retrieved 2020-20-05.

[5] S. Evans, "Dielectric properties of ice and snow - a review," *Journal of Glaciology*, 1965.

[6] M. Tom, U. Kälin, M. Sütterlin, E. Baltsavias, and K. Schindler, "Lake ice detection in low-resolution optical satellite images," *ISPRS Annals of Photogrammetry, Remote Sensing and Spatial Information Sciences*, vol. IV-2, 2018.

[7] H. J. Hendricks Franssen and S. C. Scherrer, "Freezing of lakes on the swiss plateau in the period 19012006," *International Journal of Climatology*, vol. 28, no. 4, 2008.

[8] M. Xiao, M. Rothermel, M. Tom, S. Galliani, E. Baltsavias, and K. Schindler, "Lake ice monitoring with webcams," *ISPRS Annals of Photogrammetry, Remote Sensing and Spatial Information Sciences*, vol. IV-2, 2018.

[9] L.-C. Chen, Y. Zhu, G. Papandreou, F. Schroff, and H. Adam, "Encoder-decoder with atrous separable convolution for semantic image segmentation," in *European Conference on Computer Vision*, 2018.

[10] "Esa sentinel user guides - sentinel-1 mission summary." `https://sentinel.esa.int/web/sentinel/missions/sentinel-1/overview/mission-summary`. Retrieved 2020-12-05.

[11] "Esa sentinel user guides - sentinel-1 overview." `https://sentinel.esa.int/web/sentinel/missions/sentinel-1/overview`. Retrieved 2020-12-05.

[12] "Esa sentinel user guides - sentinel-2 satellite description." ://sentinel.esa.int/web/sentinel/missions/sentinel-2/satellite-description.

[13] A. Moreira, P. Prats-Iraola, M. Younis, G. Krieger, I. Hajnsek, and K. Papathanassiou, "A tutorial on synthetic aperture radar," *Canadian Journal of Remote Sensing*, vol. 1, no. 1, pp. 6–43, 2013.

[14] J. Albertz, *Einführung in die Fernerkundung (*. WBG, 2009.

[15] "Esa sentinel user guides - sentinel-1 acquisition modes." `https://sentinel.esa.int/web/sentinel/user-guides/sentinel-1-sar/acquisition-modes`. Retrieved 2020-12-05.

[16] "Esa sentinel user guides - level-1 slc products." `https://sentinel.esa.int/web/sentinel/technical-guides/sentinel-1-sar/products-algorithms/level-1-algorithms/single-look-complex`. Retrieved 2020-12-05.

[17] J. Johannessen, G. Digranes, H. Esdedal, O. Johannessen, P. Samuel, D. Browne, and P. Vachon, "Ers-1 sar ocean feature catalogue," *ESA SP-1174*, 1994.

[18] M. Tom, R. Aguilar, P. Imhof, S. Leinss, E. Baltsavias, and K. Schindler, "Lake ice detection from sentinel-1 sar with deep learning," in *arXiv preprint: arXiv:2002.07040*, 2020.

[19] "Esa sentinel user guides - sentinel-2 msi processing levels." `https://sentinel.esa.int/web/sentinel/user-guides/sentinel-2-msi/processing-levels`. Retrieved 2020-12-05.

[20] "Esa sentinel user guides - sentinel-2 product types." `https://sentinel.esa.int/web/sentinel/user-guides/sentinel-2-msi/product-types`. Retrieved 2020-12-05.

[21] N. Gorelick, M. Hancher, M. Dixon, S. Ilyushchenko, D. Thau, and R. Moore, "Google earth engine: Planetary-scale geospatial analysis for everyone," *Remote Sensing of Environment*, vol. 202, 2017.

[22] W. Albright, "Sar noise." Retrieved from `http://www2.gi.alaska.edu/~rgens/teaching/asf_seminar/2002/sar_noise_floor.pdf`. 2020-12-05.

[23] N. Miranda, "Radiometric calibration of s-1 level-1 products generated by the s-1 ipf," 2015.

[24] "Radar image distortions." https://www.nrcan.gc.ca/maps-tools-publications/satellite-imagery-air-photos/remote-sensing-tutorials/microwave-remote-sensing/radar-image-distortions/9325, 2015. Retrieved 2020-12-05.

[25] H. Xiaotong, "Support vector machine and its application to regression and classification," 2017.

[26] G. James, D. Witten, T. Hastie, and R. Tibshirani, *An Introduction to Statistical Learning*. Springer, 2009.

[27] R. Prabha, "Ice monitoring in alpine lakes using webcam and crowd-sourced data," 2019.

[28] J. Long, E. Shelhamer, and T. Darrell, "Fully convolutional networks for semantic segmentation," in *The IEEE Conference on Computer Vision and Pattern Recognition (CVPR)*, June 2015.

[29] C. Duguay, T. Prowse, B. Bonsal, R. Brown, M. Lacroix, and P. Menard, "Recent trends in canadian lake ice cover," *Hydrological Processes*, vol. 20, no. 4, 2006.

[30] L. C. Brown and C. R. Duguay, "The response and role of ice cover in lake-climate interactions," *Progress in Physical Geography: Earth and Environment*, vol. 34, no. 5, 2010.

[31] L. C. Brown and C. R. Duguay, "The fate of lake ice in the north american arctic," *The Cryosphere*, vol. 5, no. 4, 2011.

[32] C. R. Duguay and P. M. Lafleur, "Determining depth and ice thickness of shallow sub-arctic lakes using space-borne optical and sar data," *International Journal of Remote Sensing*, vol. 24, no. 3, 2003.

[33] C. M. Surdu, C. R. Duguay, L. C. Brown, and D. Fernández Prieto, "Response of ice cover on shallow lakes of the north slope of alaska to contemporary climate conditions (1950–2011): Radar remote-sensing and numerical modeling data analysis," *The Cryosphere*, vol. 8, no. 1, 2014.

[34] S. Leigh, Z. Wang, and D. A. Clausi, "Automated icewater classification using dual polarization sar satellite imagery," *Transactions on Geoscience and Remote Sensing*, vol. 52, no. 9, 2014.

[35] C. M. Surdu, C. R. Duguay, H. K. Pour, and L. C. Brown, "Ice freeze-up and break-up detection of shallow lakes in northern alaska with spaceborne sar," *Remote Sensing*, vol. 7, no. 5, 2015.

[36] S. Antonova, C. Duguay, A. Kääb, B. Heim, M. Langer, S. Westermann, and J. Boike, "Monitoring bedfast ice and ice phenology in lakes of the lena river delta using terrasar-x backscatter and coherence time series," *Remote Sensing*, vol. 8, no. 11, 2016.

[37] J. Du, J. S. Kimball, C. Duguay, Y. Kim, and J. D. Watts, "Satellite microwave assessment of northern hemisphere lake ice phenology from 2002 to 2015," *The Cryosphere*, vol. 11, no. 1, 2017.

[38] G. Pointner, A. Bartsch, B. C. Forbes, and T. Kumpula, "The role of lake size and local phenomena for monitoring ground-fast lake ice," *International Journal of Remote Sensing*, vol. 40, no. 3, 2018.

[39] Y.-L. Tsai, A. Dietz, N. Oppelt, and C. Kuenzer, "Wet and dry snow detection using sentinel-1 sar data for mountainous areas with a machine learning technique," *Remote Sensing*, vol. 11, no. 8, 2019.

[40] C. Duguay and J. Wang, "Advancement in bedfast lake ice mapping from Sentinel-1 SAR data," in *International Geoscience and Remote Sensing Symposium*, 2019.

[41] T. Geldsetzer, J. van der Sanden, and B. Brisco, "Monitoring lake ice during spring melt using radarsat-2 sar," *Canadian Journal of Remote Sensing*, vol. 36, no. S2, 2010.

[42] J. Murfitt, L. Brown, and S. Howell, "Evaluating radarsat-2 for the monitoring of lake ice phenology events in mid-latitudes," *Remote Sensing*, vol. 10, no. 10, 2018.

[43] J. Wang, C. R. Duguay, D. A. Clausi, V. Pinard, and S. E. L. Howell, "Semi-automated classification of lake ice cover using dual polarization radarsat-2 imagery," *Remote Sensing*, vol. 10, no. 11, 2018.

[44] G. Gunn, C. R. Duguay, D. K. Atwood, J. King, and P. Toose, "Observing scattering mechanisms of bubbled freshwater lake ice using polarimetric RADARSAT-2 (c-band) and uw-scat (X- and ku-bands)," *Transactions on Geoscience and Remote Sensing*, vol. 56, no. 5, 2018.

[45] L. Wang, K. A. Scott, and D. A. Clausi, "Sea ice concentration estimation during freeze-up from sar imagery using a convolutional neural network," *Remote Sensing*, vol. 9, no. 5, 2017.

[46] R. Prabha, M. Tom, M. Rothermel, E. Baltsavias, L. Leal-Taixe, and K. Schindler in *arXiv preprint: arXiv:2002.07875*.

[47] K. Barbieux, A. Charitsi, and B. Merminod, "Icy lakes extraction and water-ice classification using landsat 8 oli multispectral data," *International Journal of Remote Sensing*, vol. 39, no. 11, 2018.

[48] M. Tom, M. Suetterlin, D. Bouffard, M. Rothermel, S. Wunderle, and E. Baltsavias, "Integrated monitoring of ice in selected swiss lakes," *Final Project Report*, 2019.

[49] M. Everingham, S. M. A. Eslami, L. Van Gool, C. K. I. Williams, J. Winn, and A. Zisserman, "The pascal visual object classes challenge: A retrospective," *International Journal of Computer Vision*, vol. 111, no. 1, 2015.

[50] M. Cordts, M. Omran, S. Ramos, T. Rehfeld, M. Enzweiler, R. Benenson, U. Franke, S. Roth, and B. Schiele, "The Cityscapes dataset for semantic urban scene understanding," in *Computer Vision and Pattern Recognition*, 2016.

[51] F. Pedregosa, G. Varoquaux, A. Gramfort, V. Michel, B. Thirion, O. Grisel, M. Blondel, P. Prettenhofer, R. Weiss, V. Dubourg, J. Vanderplas, A. Passos, D. Cournapeau, M. Brucher, M. Perrot, and E. Duchesnay, "Scikit-learn: Machine learning in Python," *Journal of Machine Learning Research*, vol. 12, pp. 2825–2830, 2011.

Appendix A

Appendices

A.1 Wind measurements

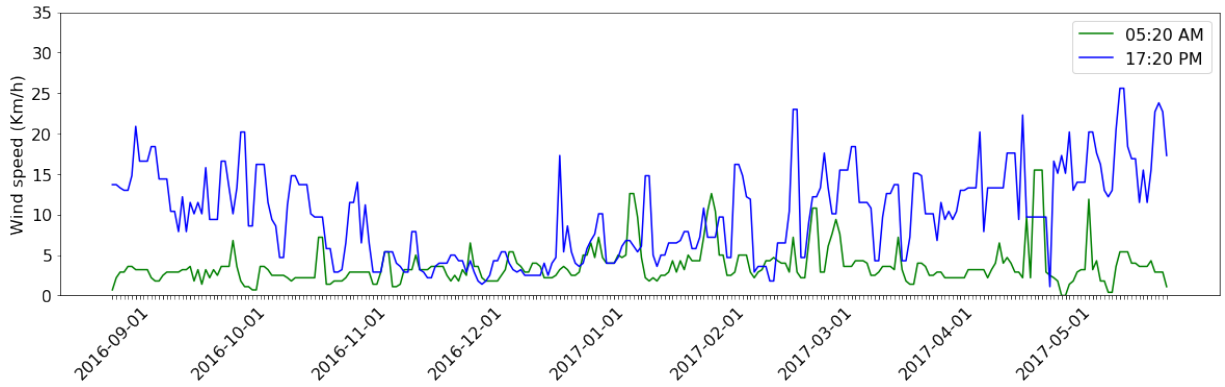

(a) $2016 - 17$

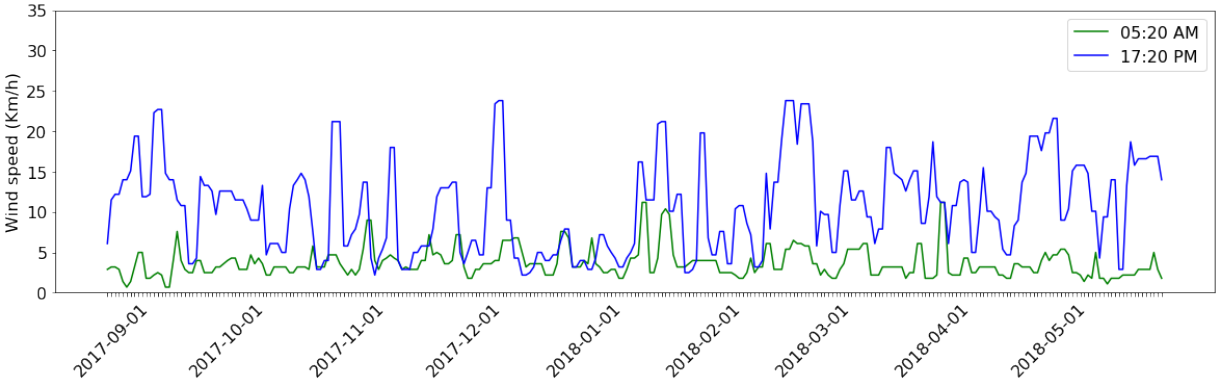

(b) $2017 - 18$

Figure A.1: Wind measurements at 05:20 and 17:20 UTC from Samedan station for winters 2016-17 and 2017-18

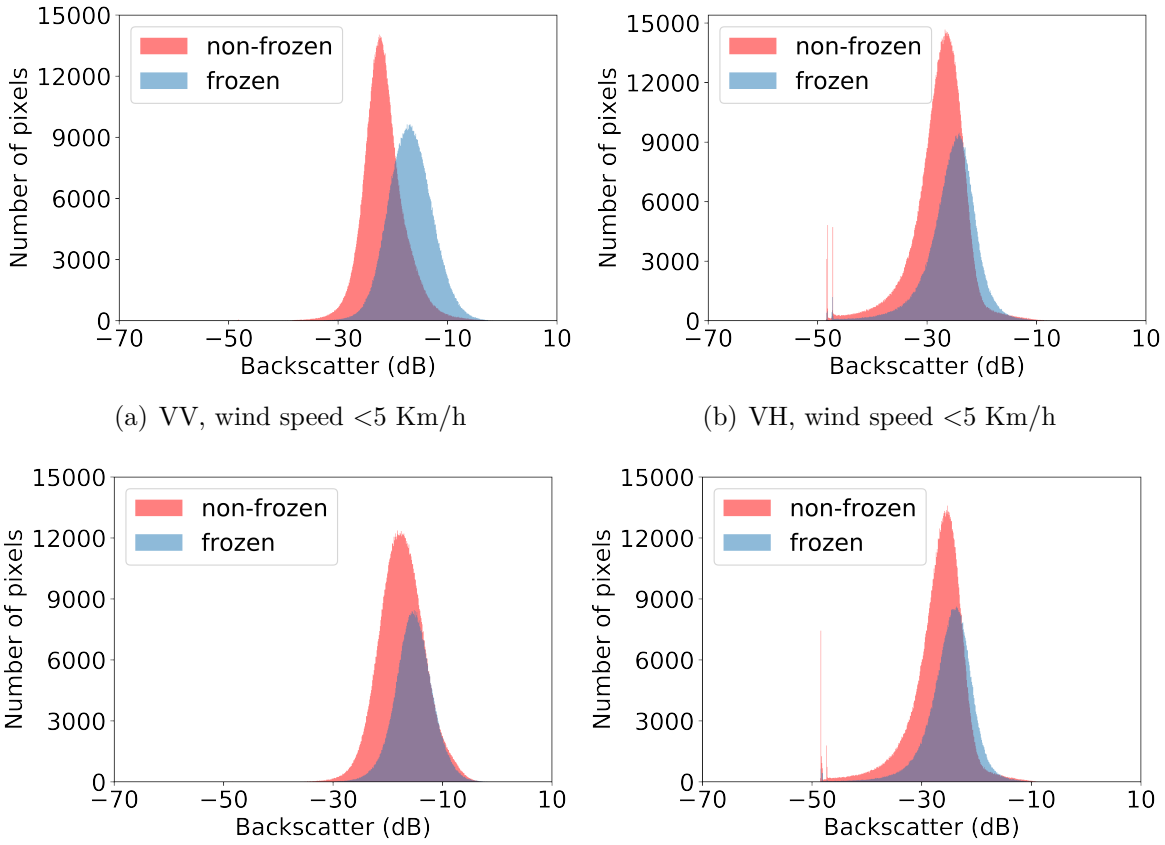

(a) VV, wind speed <5 Km/h

(b) VH, wind speed <5 Km/h

(c) VV, wind speed >20 Km/h

(d) VH, wind speed >20 Km/h

Figure A.2: Distribution of frozen and non-frozen pixels for VV and VH polarisations in different wind speed condtions on Region Sils, along 2 winters. Best if viewed on screen.

A.2 Detailed experimentation Sentinel-1

Table A.1: Results from Sentinel-1 of different training sets with validation on lake Sihl during winter 2016-17. Each row contains results per every training set with $40K$ steps during training process. *NF* stands for Non-frozen and *F* for frozen. Best mIoU in green, worst mIoU in red.

Lake	Winter	Recall		Precision		IoU			Accuracy
		NF	F	NF	F	NF	F	Mean	
Sihl	2016-17								
	2017-18	99.4	37.1	83.4	99.9	83.0	37.1	60.1	85.0
Sils	2016-17	90.0	71.8	91.0	70.4	82.6	55.1	68.9	86.0
	2017-18	98.7	43.0	84.6	94.4	83.7	42.0	62.8	85.7
Silvaplana	2016-17	89.7	86.4	94.5	73.0	85.3	65.5	75.4	89.7
	2017-18	99.1	66.7	89.9	97.0	89.1	65.4	77.3	91.6
St. Moritz	2016-17	98.2	35.0	82.1	96.1	80.9	34.5	57.7	84.2
	2017-18	96.9	61.5	88.6	88.7	86.2	57.0	71.6	89.1

Table A.2: Resultson Sentinel-1 of different training sets with validation on lake Sihl during winter 2017-18. *NF* stands for Non-frozen and *F* for frozen. Best mIoU in green, worst mIoU in red.

Lake	Winter	Recall		Precision		IoU			Accuracy
		NF	F	NF	F	NF	F	Mean	
Sihl	2016-17	98.1	29.9	89.4	76.1	87.9	27.3	57.6	88.9
	2017-18								
Sils	2016-17	87.7	78.1	95.6	51.6	84.6	45.1	64.9	86.7
	2017-18	82.7	92.5	97.0	45.0	80.1	45.2	63.0	84.7
Silvaplana	2016-17	82.7	92.5	97.0	47.0	80.1	45.3	63.0	84.8
	2017-18	98.1	37.3	90.0	79.0	88.4	34.0	61.2	89.9
St. Moritz	2016-17	97.8	29.2	88.6	84	86.8	27.7	57.2	89.4
	2017-18	97.3	40	90.4	76.4	88.2	35.6	61.9	89.9

Table A.3: Resultson Sentinel-1 of different training sets with validation on lake Sils during winter 2016-17. *NF* stands for Non-frozen and *F* for frozen. Best mIoU in green, worst mIoU in red.

Lake	Winter	Recall		Precision		IoU			Accuracy
		NF	F	NF	F	NF	F	Mean	
Sihl	2016-17	93.2	22.3	59.0	74.0	56.6	20.7	38.6	61.3
	2017-18	99.0	5.1	56.0	100	55.7	5.1	30.4	57.1
Sils	2016-17								
	2017-18	99.4	75.5	83.8	100	83.4	75.5	79.4	89.4
Silvaplana	2016-17	99.5	90.4	92.5	99.5	92.1	90.0	91.0	96.3
	2017-18	99.4	86.0	89.7	99.6	89.2	85.7	87.5	93.9
St. Moritz	2016-17	98.0	61.0	75.7	98.9	74.5	60.6	67.5	82.8
	2017-18	98.6	71.9	80.6	98.2	79.7	71	75.4	87

Table A.4: Results from Sentinel-1 of different training sets with validation on lake Sils during winter 2017-18. *NF* stands for Non-frozen and *F* for frozen. Best mIoU in green, worst mIoU in red.

Lake	Winter	Recall		Precision		IoU			Accuracy
		NF	F	NF	F	NF	F	Mean	
Sihl	2016-17	90.1	23.1	57.7	67.5	54.3	20.8	37.5	59.5
	2017-18	99.1	7.8	56.1	100	55.8	7.8	31.8	57.7
Sils	2016-17	99.7	89.5	91.9	99.9	91.6	89.4	90.5	95.3
	2017-18								
Silvaplana	2016-17	98.9	88.5	91.0	98.7	90.0	87.5	88.8	95.0
	2017-18	98.1	93.7	94.9	98.2	93.2	92.1	92.7	96.6
St. Moritz	2016-17	97.8	73.2	81.7	98.8	80.2	72.6	76.4	88.1
	2017-18	97.5	84.4	87.7	96.9	85.8	82.2	84.0	92

Table A.5: Results from Sentinel-1 of different training sets with validation on lake Silvaplana during winter 2016-17. *NF* stands for Non-frozen and *F* for frozen. Best mIoU in green, worst mIoU in red.

Lake	Winter	Recall		Precision		IoU			Accuracy
		NF	F	NF	F	NF	F	Mean	
Sihl	2016-17	95.6	19.3	58.7	79.4	57.2	18.4	37.8	61.2
	2017-18	99.2	0.9	54.9	100	54.7	0.9	27.8	55.1
Sils	2016-17	99.7	66.5	78.3	99.9	78	66.4	72.2	84.9
	2017-18	99.5	35.4	65.3	100	65.1	35.4	50.3	71.0
Silvaplana	2016-17								
	2017-18	98.8	78.8	85.3	99	84.4	78.2	81.3	90.3
St. Moritz	2016-17	98.0	37.8	65.8	97.3	64.9	37.4	51.2	71.7
	2017-18	95.4	70.4	79.5	93.4	76.6	67	71.8	84.5

Table A.6: Results from Sentinel-1 of different training sets with validation on lake Silvaplana during winter 2017-18. *NF* stands for Non-frozen and *F* for frozen. Best mIoU in green, worst mIoU in red.

Lake	Winter	Recall		Precision		IoU			Accuracy
		NF	F	NF	F	NF	F	Mean	
Sihl	2016-17	95.7	31.4	64.2	85.9	62.4	29.9	46.1	67.8
	2017-18	99.2	1.7	56.8	100	56.6	1.7	29.2	57.2
Sils	2016-17	99.7	63.9	78.1	99.9	77.9	63.9	70.9	84.4
	2017-18	99.4	58.9	76.2	100	75.8	58.9	67.4	82.4
Silvaplana	2016-17	99.7	69.4	81	99.9	80.8	69.3	75.1	87.1
	2017-18								
St. Moritz	2016-17	98.0	14.8	59.8	92.8	59.1	14.6	36.9	62.5
	2017-18	95.4	81.7	87.1	93.8	83.5	77.5	80.5	89.9

Table A.7: Results from Sentinel-1 of different training sets with validation on lake St. Moritz during winter 2016-17. *NF* stands for Non-frozen and *F* for frozen. Best mIoU in green, worst mIoU in red.

Lake	Winter	Recall		Precision		IoU			Accuracy
		NF	F	NF	F	NF	F	Mean	
Sihl	2016-17	97.5	7.8	62.4	71.8	61.4	7.5	34.5	63.0
	2017-18	98.6	0	61.1	0	60.6	0	30.3	61.2
Sils	2016-17	96.1	83.4	90.4	94.2	87.2	79.4	83.3	91.9
	2017-18	99.2	34.4	71.0	99.9	70.6	34.4	52.5	75.0
Silvaplana	2016-17	99.1	64.5	82.1	99.9	81.5	64.4	73.0	87.4
	2017-18	91.7	81.6	89.5	88.2	82.8	73.5	78.2	89.1
St. Moritz	2016-17								
	2017-18	96.9	87.3	92.3	95.6	89.7	84	86.9	93.8

Table A.8: Results from Sentinel-1 of different training sets with validation on lake St. Moritz during winter 2017-18. *NF* stands for Non-frozen and *F* for frozen. Best mIoU in green, worst mIoU in red.

Lake	Winter	Recall		Precision		IoU			Accuracy
		NF	F	NF	F	NF	F	Mean	
Sihl	2016-17	99.1	2.7	52.5	85.4	52.3	2.7	27.5	53.3
	2017-18	98.6	0	61.1	0	60.6	0	30.3	61.2
Sils	2016-17	95.9	82.8	86.2	95.4	83.1	79.6	81.4	90.3
	2017-18	99.2	65.7	77.1	99.9	76.7	65.7	71.2	84.5
Silvaplana	2016-17	99.1	71.7	80.8	99.9	80.3	71.7	76	88.2
	2017-18	92.7	92.2	94.1	93.5	87.6	86.6	87.1	93.9
St. Moritz	2016-17	98.9	77.6	83.8	99.7	83.1	77.5	80.3	90.1
	2017-18								

A.3 Detailed experimentation Sentinel-2

Table A.9: Results from Sentinel-2 of different training sets with validation on lake Sihl during winter 2016-17. *NF* stands for Non-frozen and *F* for frozen. Best mIoU in green, worst mIoU in red.

Lake	Winter	Recall		Precision		IoU			Accuracy
		NF	F	NF	F	NF	F	Mean	
Sihl	2016-17								
	2017-18	99.7	81.3	95.3	81.3	95	80.2	87.6	95.9
Sils	2016-17	99.9	68.3	90.5	68.3	90.4	68.2	79.3	92.0
	2017-18	99.7	98.9	99.8	98.9	99.5	97.7	98.6	99.6
Silvaplana	2016-17	99.9	46.6	76.4	46.6	76.4	46.6	61.5	80.4
	2017-18	99.6	99.9	100	99.9	99.5	97.8	98.7	99.6
St. Moritz	2016-17	99.9	92	98.2	92	98.1	91.7	94.9	98.5
	2017-18	99.8	98.8	99.8	98.8	99.5	97.7	98.6	99.6

Table A.10: Results of different training sets with validation on lake Sils during winter 2016-17. *NF* stands for Non-frozen and *F* for frozen. Best mIoU in green, worst mIoU in red.

Lake	Winter	Recall		Precision		IoU			Accuracy
		NF	F	NF	F	NF	F	Mean	
Sihl	2016-17	89.2	98.3	99.3	98.3	88.6	76.8	82.7	91.7
	2017-18	87.6	78.3	88.4	78.3	78.5	63.5	71.0	84.4
Sils	2016-17								
	2017-18	86.7	99.6	99.8	99.6	86.6	71.7	79.1	90
Silvaplana	2016-17	99.2	87.2	92.1	87.2	91.4	86.2	88.8	94.4
	2017-18	84.7	99.8	99.9	99.8	84.7	66.8	75.8	88.3
St. Moritz	2016-17	96.3	95.6	97.7	95.6	94.2	89.3	91.7	96.1
	2017-18	89.4	99.5	99.8	99.5	89.2	77.9	83.6	92.2

Table A.11: Results of different training sets with validation on lake Silvaplana during winter 2016-17. *NF* stands for Non-frozen and *F* for frozen. Best mIoU in green, worst mIoU in red.

Lake	Winter	Recall		Precision		IoU			Accuracy
		NF	F	NF	F	NF	F	Mean	
Sihl	2016-17	86.3	98.6	99.4	98.6	85.8	71.6	78.7	89.5
	2017-18	89.3	83.8	91.1	83.8	82.1	69.9	76.0	87.3
Sils	2016-17	93.2	98.8	99.4	98.8	92.7	86.4	89.5	95
	2017-18	85.6	99.1	99.6	99.1	85.3	70.3	77.8	89.1
Silvaplana	2016-17								
	2017-18	83.1	99.4	99.8	99.4	82.9	64.2	73.6	86.9
St. Moritz	2016-17	91.6	98.4	99.2	98.4	90.9	82.9	86.9	93.7
	2017-18	86.5	98.9	99.5	98.9	86.2	72.3	79.2	89.8

Table A.12: Results from Sentinel-2 of different training sets with validation on lake St. Moritz during winter 2016-17. *NF* stands for Non-frozen and *F* for frozen. Best mIoU in green, worst mIoU in red.

Lake	Winter	Recall		Precision		IoU			Accuracy
		NF	F	NF	F	NF	F	Mean	
Sihl	2016-17	67.4	97.9	99.2	97.9	67.1	42.2	54.6	73.5
	2017-18	71.7	81.7	89.2	81.7	65.9	51.1	58.5	74.9
Sils	2016-17	73.7	98.5	99.3	98.5	73.3	57	65.2	80.3
	2017-18	66.7	98.6	99.5	98.6	66.5	40.1	53.3	72.6
Silvaplana	2016-17	73.9	97.6	98.8	97.6	73.3	57.3	65.3	80.3
	2017-18	66.0	99.6	99.9	99.6	66	38.3	52.2	71.9
St. Moritz	2016-17								
	2017-18	68.9	98.4	99.4	98.4	68.6	45.8	57.2	75.2

Table A.13: Results from Sentinel-2 of different training sets with validation on lake Sihl during winter 2017-18. *NF* stands for Non-frozen and *F* for frozen. Best mIoU in green, worst mIoU in red.

Lake	Winter	Recall		Precision		IoU			Accuracy
		NF	F	NF	F	NF	F	Mean	
Sihl	2016-17	93.3	18.1	92.5	18.1	86.8	10.5	48.6	87.0
	2017-18								
Sils	2016-17	95.1	53.2	97	53.2	92.5	29.8	61.1	92.7
	2017-18	92.9	54.5	99.5	54.5	92.4	7.4	49.9	92.4
Silvaplana	2016-17	95.5	32.9	91.8	32.9	88	24.3	56.2	88.5
	2017-18	92.9	68.7	99.7	68.7	92.6	7.7	50.2	92.7
St. Moritz	2016-17	95.2	71.8	98.7	71.8	94	35.1	64.6	94.2
	2017-18	93.1	57.5	99.3	57.5	92.5	11.1	51.8	92.6

Table A.14: Results from Sentinel-2 of different training sets with validation on lake Sils during winter 2017-18. *NF* stands for Non-frozen and *F* for frozen. Best mIoU in green, worst mIoU in red.

Lake	Winter	Recall		Precision		IoU			Accuracy
		NF	F	NF	F	NF	F	Mean	
Sihl	2016-17	99.8	97.5	98.2	97.5	98.0	97.2	97.6	98.8
	2017-18	98.9	91.4	93.4	91.4	92.5	90.3	91.4	95.6
Sils	2016-17	99.9	86.3	88.7	86.3	88.6	86.2	87.4	93.3
	2017-18								
Silvaplana	2016-17	99.9	83.6	86.1	83.6	86	83.5	84.8	91.8
	2017-18	99.6	99.8	99.9	99.8	99.4	99.2	99.3	99.7
St. Moritz	2016-17	100	84.2	86.6	84.2	86.6	84.1	85.4	92.2
	2017-18	99.9	99.3	99.5	99.3	99.4	99.1	99.2	99.6

Table A.15: Results from Sentinel-2 of different training sets with validation on lake Silvaplana during winter 2017-18. *NF* stands for Non-frozen and *F* for frozen. Best mIoU in green, worst mIoU in red.

Lake	**Winter**	**Recall**		**Precision**		**IoU**			**Accuracy**
		NF	**F**	**NF**	**F**	**NF**	**F**	**Mean**	
Sihl	2016-17	99.9	98.2	98.9	98.2	98.8	98	98.4	99.2
	2017-18	95	96.2	97.9	96.2	93	88.2	90.6	95.4
Sils	2016-17	100	83.9	88.5	83.9	88.5	83.9	86.2	92.8
	2017-18	98.8	99.4	99.7	99.4	98.5	97.5	98.0	99.0
Silvaplana	2016-17	100	79.6	84.6	79.6	84.6	79.5	82.1	90.4
	2017-18								
St. Moritz	2016-17	100	82.6	87.4	82.6	87.4	82.6	85.0	92.1
	2017-18	99.8	99	99.4	99	99.3	98.8	99.0	99.5

Table A.16: Results from Sentinel-2 of different training sets with validation on lake St. Moritz during winter 2017-18. *NF* stands for Non-frozen and *F* for frozen. Best mIoU in green, worst mIoU in red.

Lake	**Winter**	**Recall**		**Precision**		**IoU**			**Accuracy**
		NF	**F**	**NF**	**F**	**NF**	**F**	**Mean**	
Sihl	2016-17	99.1	99.2	99.5	99.2	98.6	97.7	98.1	99.1
	2017-18	98.7	95.5	97.2	95.5	96	93.5	94.7	97.4
Sils	2016-17	99.7	84.9	89.3	84.9	89	84.5	86.8	93.1
	2017-18	99.2	99.7	99.8	99.7	99	98.3	98.7	99.4
Silvaplana	2016-17	99.6	81.4	86.3	81.4	86	81	83.5	91.2
	2017-18	98.4	99.9	99.9	99.9	98.3	97.2	97.8	98.9
St. Moritz	2016-17	99.8	83.5	88.1	83.5	87.9	83.3	85.6	92.5
	2017-18								

A.4 Summary of daily results for all monitoring data and lakes Sihl, Sils, Silvaplana, and St. Mortiz in the winters 2016-17 and 2017-18

Table A.17: Prediction per day: Sihl 2016-17

Date	Sentinel 1	Sentinel 2
01.09	100	
02.09		100
09.09		99
12.09		100
13.09	100	
22.09		100
25.09	100	
26.09	100	
29.09		100
30.09	100	
07.10	100	
12.10		100
19.10	100	
22.10		100
29.10		100
31.10	100	
01.11		100
08.11		97
12.11	100	
24.11	100	
01.12		100
06.12	100	
08.12		98
18.12	100	98
21.12		93

30.12	99	
07.01		0
11.01	0	
23.01	0	
27.01		0
04.02	0	
16.02	0	1
19.02		1
28.02	100	
04.03	99	
07.03	82	
11.03		25
12.03	100	
13.03	100	
17.03	100	
24.03	100	
25.03	100	
28.03		100
29.03	100	
31.03	100	
05.04	100	
06.04	100	
07.04		100
10.04	100	100
12.04	100	
17.04	100	
18.04	100	
22.04	100	
24.04	100	
29.04	100	
30.04	100	
04.05	100	
06.05	100	

10.05		100
11.05	100	
12.05	100	
16.05	100	
17.05		99
18.05	100	
23.05	100	
24.05	100	
27.05		100
28.05	100	

Table A.18: Prediction per day: Sihl 2017-18

Date	Sentinel 1	Sentinel 2
01.09	100	
03.09	100	
08.09	100	
09.09	100	
13.09	99	
15.09	100	
20.09	100	
21.09	100	
24.09		89
25.09	100	
27.09	100	6
02.10	100	
03.10	100	
07.10	100	94
09.10	100	
14.10	100	95
15.10	100	
17.10		95
19.10	100	

21.10	100	
24.10		85
26.10	100	
27.10	100	
31.10	100	
02.11	100	
03.11		94
07.11	100	
08.11	100	
12.11	100	
14.11	100	
18.11	100	
20.11	100	
24.11	100	
26.11	100	
30.11	100	
02.12	100	
03.12		93
06.12	100	93
08.12	100	
12.12	100	
13.12		86
18.12	100	
21.12		85
23.12		72
24.12	91	
26.12	0	
30.12	0	
31.12		57
01.01	99	
05.01	100	
07.01	100	
11.01	100	

13.01	99	
19.01	100	
23.01	100	
25.01	100	
29.01	100	
31.01	100	
04.02	100	
06.02	87	
09.02		60
10.02	100	
12.02	0	
16.02	91	
18.02	0	
22.02	0	
24.02	0	
28.02	0	
02.03	0	
06.03	0	
08.03	0	
12.03	99	
14.03	95	
18.03	89	
20.03	100	
24.03	87	
26.03	100	
30.03	100	
01.04	100	
05.04	100	
07.04	100	
11.04	100	
13.04	100	
19.04	100	
20.04		78

23.04	100	
25.04	100	
30.04		37
01.05	100	
05.05	100	
07.05	100	
11.05	100	
12.05		81
13.05	100	
17.05	100	
19.05	100	
23.05	100	
25.05	100	26
29.05	100	

Table A.19: Prediction per day: Sils 2016-17

Date	Sentinel 1	Sentinel 2
01.09	100	
05.09	100	
08.09	100	
09.09		100
12.09	100	
13.09	100	
17.09	100	
20.09	100	
24.09	97	
25.09	100	
26.09	100	
29.09	100	100
30.09	100	
02.10	100	
06.10	62	

07.10	100	
11.10	100	
14.10	100	
18.10	99	
19.10	100	
23.10	100	
26.10	100	
29.10		100
30.10	99	
31.10	100	
04.11	100	
07.11	10	
08.11		96
11.11	100	
12.11	100	
16.11	100	
19.11	100	
24.11	100	
28.11	100	99
01.12	100	
05.12	99	
06.12	100	
08.12		99
10.12	100	
13.12	100	
17.12	99	
18.12	100	99
22.12	100	
25.12	100	
28.12		99
29.12	61	
30.12	100	
03.01	100	

06.01	0	
07.01		15
10.01	0	
11.01	0	
15.01	0	
18.01	0	
23.01	0	
27.01	0	6
30.01	0	
03.02	0	
04.02	0	
08.02	0	
11.02	0	
15.02	0	
16.02	0	1
20.02	0	
23.02	0	
27.02	0	
28.02	0	
04.03	0	
06.03	0	
07.03	0	
10.03	0	
11.03	0	
12.03	0	
13.03	0	
16.03	0	
17.03	0	
18.03	0	
19.03	0	
23.03	2	
24.03	13	
25.03	0	

28.03	0	3
29.03	0	
30.03	0	
31.03	0	
03.04	0	
04.04	7	
05.04	0	
06.04	0	
07.04		60
09.04	0	
10.04	0	
11.04	7	
12.04	99	
15.04	100	
16.04	100	
17.04	100	100
18.04	100	
21.04	100	
22.04	100	
23.04	100	
24.04	100	
27.04	100	
28.04	100	
29.04	100	
30.04	100	
03.05	100	
04.05	100	
05.05	100	
06.05	100	
09.05	100	
10.05	100	
11.05	100	
12.05	100	

15.05	100	
16.05	100	
17.05	100	
18.05	100	
21.05	100	
22.05	100	
23.05	100	
24.05	100	
27.05	100	100
28.05	100	
29.05	100	
30.05	100	

Table A.20: Prediction per day: Sils 2017-18

Date	Sentinel 1	Sentinel 2
01.09	50	
02.09	100	
03.09	100	
06.09	100	
07.09	100	
08.09	100	
09.09	100	
12.09	100	
13.09	100	
14.09	100	
15.09	100	
18.09	100	
19.09	94	
20.09	100	
21.09	100	
24.09	100	81
25.09	100	

26.09	100	
27.09	100	
30.09	100	
01.10	100	
02.10	100	
03.10	100	
04.10		99
06.10	100	
07.10	8	
08.10	100	
09.10	100	99
12.10	100	
13.10	100	
14.10	100	
15.10	100	
18.10	100	
19.10	100	100
20.10	100	
21.10	100	
24.10	100	99
25.10	100	
26.10	100	
27.10	100	
30.10	100	
31.10	100	
01.11	100	
02.11	100	
03.11		99
05.11	100	
06.11	100	
07.11	100	
08.11	100	0
11.11	100	

12.11	100	
13.11	91	
14.11	100	
17.11	100	
18.11	100	97
19.11	100	
20.11	100	
23.11	100	
24.11	100	
25.11	100	
26.11	100	
29.11	100	
30.11	100	
01.12	99	
02.12	100	
03.12		97
05.12	100	
06.12	87	
07.12	99	
08.12	99	
11.12	100	
12.12	100	
13.12	100	66
14.12	100	
17.12	90	
18.12	30	0
19.12	33	
20.12	1	
23.12	0	
24.12	2	
25.12	0	
26.12	52	
29.12	0	

30.12	0	
31.12	0	
01.01	0	
04.01	0	
05.01	0	
06.01	0	
07.01	0	
10.01	0	
11.01	0	
12.01	0	0
13.01	0	
16.01	0	
17.01	0	
18.01	0	
19.01	0	
22.01	0	
23.01	0	
24.01	0	
25.01	0	
28.01	0	
29.01	0	
30.01	0	
31.01	0	
03.02	0	
04.02	0	
05.02	0	
06.02	0	
09.02	0	
10.02	0	
11.02	0	
12.02	0	
15.02	0	
16.02	0	0

17.02	0	
18.02	0	
21.02	0	0
22.02	0	
23.02	0	
24.02	0	
27.02	0	
28.02	0	
01.03	0	
02.03	0	
05.03	0	
06.03	0	
07.03	0	
08.03	0	
11.03	0	
12.03	0	
13.03	0	0
14.03	0	
17.03	0	
18.03	0	
19.03	0	
20.03	0	
23.03	0	
24.03	0	
25.03	0	
26.03	0	
29.03	42	
30.03	100	
31.03	99	
01.04	99	
02.04		0
04.04	0	
05.04	93	

06.04	100	
07.04	100	0
10.04	100	
11.04	100	
12.04	100	
13.04	100	
16.04	100	
17.04	100	0
19.04	47	
22.04	0	0
23.04	0	
24.04	0	
25.04	5	
28.04	100	
29.04	26	
30.04	7	
01.05	98	
04.05	88	
05.05	9	
06.05	39	
07.05	100	97
10.05	99	
11.05	100	
12.05	100	
13.05	100	
16.05	100	
17.05	100	
18.05	100	
19.05	100	
22.05	100	
23.05	100	
24.05	100	
25.05	100	

28.05	100	
29.05	100	
30.05	100	

Table A.21: Prediction per day: Silvaplana 2016-17

Date	Sentinel 1	Sentinel 2
01.09	100	
05.09	100	
08.09	100	
09.09		100
12.09	100	
13.09	100	
17.09	100	
20.09	100	
24.09	100	
25.09	100	
26.09	100	
29.09	100	100
30.09	100	
02.10	100	
06.10	100	
07.10	100	
11.10	100	
14.10	100	
18.10	100	
19.10	100	
23.10	100	
26.10	100	
29.10		100
30.10	100	
31.10	100	
04.11	100	

07.11	21	
08.11		96
11.11	97	
12.11	100	
16.11	100	
19.11	100	
24.11	100	
28.11	100	99
01.12	100	
05.12	100	
06.12	100	
08.12		100
10.12	100	
13.12	100	
17.12	100	
18.12	100	100
22.12	100	
25.12	100	
28.12		100
29.12	100	
30.12	100	
03.01	100	
06.01	87	
10.01	83	
11.01	96	
15.01	0	
18.01	5	
23.01	65	
27.01	12	4
30.01	14	
03.02	0	
04.02	0	
08.02	0	

11.02	0	
15.02	0	
16.02	0	1
20.02	0	
23.02	0	
27.02	0	
28.02	0	
04.03	0	
06.03	0	
07.03	0	
10.03	0	
11.03	0	
12.03	0	
13.03	0	
16.03	0	
17.03	0	
18.03	16	
19.03	25	
23.03	81	
24.03	86	
25.03	0	
28.03	7	4
29.03	0	
30.03	50	
31.03	69	
03.04	2	
04.04	65	
05.04	57	
06.04	10	
07.04		78
09.04	30	
10.04	8	
11.04	0	

12.04	12	
15.04	93	
16.04	100	
17.04	100	
18.04	87	
21.04	100	
22.04	100	
23.04	100	
24.04	100	
27.04	100	
28.04	100	
29.04	100	
30.04	100	
03.05	100	
04.05	100	
05.05	100	
06.05	78	
09.05	100	
10.05	100	
11.05	100	
12.05	96	
15.05	100	
16.05	100	
17.05	99	
18.05	100	
21.05	100	
22.05	100	
23.05	100	
24.05	100	
27.05	100	100
28.05	100	
29.05	100	
30.05	86	

Table A.22: Prediction per day: Silvaplana 2017-18

Date	Sentinel 1	Sentinel 2
01.09	59	
02.09	100	
03.09	100	
04.09		91
06.09	100	
07.09	95	
08.09	97	
09.09	100	
12.09	100	
13.09	100	
14.09	40	
15.09	100	
18.09	100	
19.09	79	
20.09	100	
21.09	100	
24.09	100	
25.09	100	
26.09	98	
27.09	100	
30.09	100	
01.10	100	
02.10	100	
03.10	99	
04.10		99
06.10	100	
07.10	99	
08.10	95	
09.10	100	99
12.10	100	
13.10	96	

14.10	100	
15.10	100	
18.10	100	
19.10	100	99
20.10	100	
21.10	100	
24.10	100	99
25.10	100	
26.10	100	
27.10	100	
30.10	100	
31.10	100	
01.11	100	
02.11	100	
03.11		99
05.11	100	
06.11	33	
07.11	100	
08.11	100	0
11.11	100	
12.11	100	
13.11	87	
14.11	100	
17.11	100	
18.11	98	95
19.11	98	
20.11	99	
23.11	100	
24.11	100	
25.11	99	
26.11	100	
29.11	99	
30.11	97	

01.12	100	
02.12	99	
03.12		95
05.12	100	
06.12	100	
07.12	100	
08.12	100	
11.12	99	
12.12	68	
13.12	100	95
14.12	100	
17.12	100	
18.12	79	
19.12	99	
20.12	100	
23.12	89	
24.12	97	
25.12	96	
26.12	9	
29.12	2	
30.12	0	
31.12	0	
01.01	0	
04.01	0	
05.01	0	
06.01	0	
07.01	0	
10.01	0	
11.01	0	
12.01	0	0
13.01	17	
16.01	2	
17.01	6	

18.01	0	
19.01	33	
22.01	87	
23.01	0	
24.01	0	
25.01	0	
28.01	0	
29.01	0	
30.01	0	
31.01	0	
03.02	0	
04.02	0	
05.02	0	
06.02	0	
09.02	0	
10.02	0	
11.02	0	0
12.02	0	
15.02	0	
16.02	0	0
17.02	0	
18.02	0	
21.02	0	0
22.02	0	
23.02	0	
24.02	0	
27.02	0	
28.02	0	
01.03	0	
02.03	0	
05.03	0	
06.03	0	
07.03	0	

08.03	0	
11.03	0	
12.03	0	
13.03	91	
14.03	44	
17.03	0	
18.03	0	
19.03	0	
20.03	1	
23.03	0	
24.03	0	
25.03	0	
26.03	0	
29.03	87	
30.03	87	
31.03	94	
01.04	2	
02.04		0
04.04	11	
05.04	52	
06.04	100	
07.04	69	0
10.04	26	
11.04	0	
12.04	1	
13.04	100	
16.04	100	
17.04	12	0
19.04	93	
22.04	0	0
23.04	0	
24.04	42	
25.04	39	

28.04	100	
29.04	1	
30.04	8	
01.05	28	
04.05	100	
05.05	100	
06.05	100	
07.05	100	82
10.05	100	
11.05	100	
12.05	100	
13.05	100	
16.05	100	
17.05	100	
18.05	100	
19.05	100	
22.05	100	
23.05	100	
24.05	100	
25.05	100	
28.05	100	
29.05	100	
30.05	100	

Table A.23: Prediction per day: St. Moritz 2016-17

Date	Sentinel 1	Sentinel 2
01.09	100	
05.09	100	
08.09	100	
09.09		100
12.09	100	
13.09	100	

17.09	100	
20.09	100	
24.09	100	
25.09	100	
26.09	100	
29.09	100	100
30.09	100	
02.10	100	
06.10	100	
07.10	100	
11.10	100	
14.10	100	
18.10	100	
19.10	100	
23.10	100	
26.10	100	
29.10		100
30.10	100	
31.10	100	
04.11	100	
07.11	2	
08.11		95
11.11	90	
12.11	100	
16.11	100	
19.11	100	
24.11	100	
28.11	100	100
01.12	100	
05.12	100	
06.12	100	
08.12		100
10.12	100	

13.12	100	
17.12	93	
18.12	100	100
22.12	100	
25.12	1	
28.12		99
29.12	2	
30.12	100	
03.01	10	
06.01	22	
10.01	0	
11.01	47	
15.01	1	
18.01	0	
23.01	0	
27.01	3	12
30.01	0	
03.02	0	
04.02	0	
08.02	2	
11.02	0	
15.02	0	
16.02	1	4
20.02	8	
23.02	0	
27.02	0	
28.02	0	
04.03	0	
06.03	0	
07.03	0	
10.03	0	
11.03	0	
12.03	0	

13.03	0	
16.03	0	
17.03	1	
18.03	1	
19.03	0	
23.03	0	
24.03	0	
25.03	0	
28.03	0	11
29.03	0	
30.03	100	
31.03	42	
03.04	15	
04.04	7	
05.04	100	
06.04	100	
07.04		96
09.04	98	
10.04	100	
11.04	100	
12.04	100	
15.04	100	
16.04	100	
17.04	100	
18.04	100	
21.04	100	
22.04	100	
23.04	100	
24.04	100	
27.04	100	
28.04	44	
29.04	95	
30.04	100	

03.05	100	
04.05	100	
05.05	97	
06.05	100	
09.05	100	
10.05	100	
11.05	100	
12.05	100	
15.05	100	
16.05	100	
17.05	100	
18.05	100	
21.05	100	
22.05	100	
23.05	100	
24.05	100	
27.05	100	
28.05	100	
29.05	31	
30.05	100	

Table A.24: Prediction per day: St. Moritz 2017-18

Date	Sentinel 1	Sentinel 2
01.09	100	
02.09	100	
03.09	100	
04.09		96
06.09	100	
07.09	100	
08.09	100	
09.09	100	
12.09	100	

13.09	100	
14.09	100	
15.09	100	
18.09	100	
19.09	100	
20.09	100	
21.09	100	
24.09	100	
25.09	100	
26.09	100	
27.09	100	
30.09	100	
01.10	100	
02.10	100	
03.10	100	
04.10		99
06.10	100	
07.10	100	
08.10	100	
09.10	100	99
12.10	100	
13.10	93	
14.10	100	
15.10	100	
18.10	100	
19.10	100	99
20.10	100	
21.10	100	
24.10	100	99
25.10	100	
26.10	100	
27.10	97	
30.10	100	

31.10	100	
01.11	100	
02.11	100	
03.11		99
05.11	100	
06.11	100	
07.11	100	
08.11	100	0
11.11	100	
12.11	100	
13.11	100	
14.11	100	
17.11	100	
18.11	100	94
19.11	100	
20.11	100	
23.11	100	
24.11	100	
25.11	100	
26.11	100	
29.11	100	
30.11	100	
01.12	100	
02.12	100	
03.12		75
05.12	91	
06.12	100	
07.12	100	
08.12	99	
11.12	36	
12.12	100	
13.12	100	2
14.12	95	

17.12	100	
18.12	62	
19.12	87	
20.12	11	
23.12	0	
24.12	69	
25.12	53	
26.12	0	
29.12	0	
30.12	0	
31.12	0	
01.01	1	
04.01	1	
05.01	1	
06.01	1	
07.01	1	
10.01	1	
11.01	1	
12.01	1	0
13.01	1	
16.01	1	
17.01	0	
18.01	0	
19.01	1	
22.01	0	
23.01	1	
24.01	1	
25.01	1	
28.01	1	
29.01	1	
30.01	1	
31.01	1	
03.02	1	

04.02	0	
05.02	0	
06.02	1	
09.02	1	
10.02	0	
11.02	0	
12.02	1	
15.02	1	
16.02	1	0
17.02	0	
18.02	1	
21.02	1	0
22.02	0	
23.02	1	
24.02	1	
27.02	1	
28.02	1	
01.03	1	
02.03	1	
05.03	1	
06.03	1	
07.03	1	
08.03	1	
11.03	1	
12.03	99	
13.03	100	
14.03	100	
17.03	99	
18.03	25	
19.03	99	
20.03	0	
23.03	1	
24.03	1	

25.03	0	
26.03	1	
29.03	0	
30.03	100	
31.03	95	
01.04	100	
02.04		0
04.04	100	
05.04	100	
06.04	4	
07.04	100	0
10.04	0	
11.04	1	
12.04	11	
13.04	99	
16.04	100	
17.04	0	2
19.04	100	
22.04	4	6
23.04	1	
24.04	11	
25.04	33	
28.04	44	
29.04	3	
30.04	100	
01.05	100	
04.05	100	
05.05	100	
06.05	100	
07.05	100	62
10.05	98	
11.05	100	
12.05	100	

13.05	100	
16.05	100	
17.05	100	
18.05	100	
19.05	100	
22.05	100	
23.05	100	
24.05	100	
25.05	100	
28.05	100	
29.05	100	
30.05	100	